Multi-decadal temporal reconstruction of Sentinel-3 OLCI-based vegetation products with multi-output Gaussian process regression

Dávid D.Kovács [a,*], Pablo Reyes-Muñoz [a], Katja Berger [a,b], Viktor Ixion Mészáros [a], Gabriel Caballero [a], Jochem Verrelst [a]

[a] *IPL - University of Valencia, Catedrático Agustín Escardino Benlloch 9, Paterna 46980, Spain*
[b] *GFZ - German Research Centre for Geosciences, Telegrafenberg, Potsdam 14473, Germany*

ABSTRACT

Operational Earth observation missions, like the Sentinel-3 (S3) satellites, aim to provide imagery for long-term environmental assessment to monitor and analyze vegetation changes and dynamics. However, the S3 archive is limited in temporal availability to the year 2016. Although S3 provides continuity of previous missions, key vegetation products (VPs) including leaf area index (LAI), fraction of photosynthetically active radiation (FAPAR), fractional vegetation cover (FVC), and leaf chlorophyll content (LCC), can be reliably produced from Ocean and Land Colour Instrument (OLCI) data only since the sensors' launch. To overcome this limitation, our study proposes a reconstruction workflow that extends the data record beyond its data acquisition. By using multi-output Gaussian process regression (MOGPR) fusion, we explored guiding predictor VPs from the Moderate Resolution Imaging Spectroradiometer (MODIS) sensor for the reconstruction of multi-decadal (spanning two decades, 2002–2022) temporal profiles of four OLCI-derived VPs (S3-MOGPR), moving past S3's launch. We first evaluated three MODIS-derived inputs as predictor variables: LAI, FAPAR, and the Normalised Difference Vegetation Index (NDVI) over nine sites with distinct land covers from the Ground-Based Observations for Validation (GBOV) service. Each predictor produced a distinct time series for the four reconstructed S3 VPs. To determine which predictor variable most accurately reconstructs data streams of the targeted variable, all S3-MOGPR VPs were compared to satellite-based products from the Copernicus Global Land Service (CGLS). MOGPR models were trained for 2019 and compared to reference data. Since MODIS LAI demonstrated the best reconstruction performance of all predictors, S3-MOGPR VPs were fully reconstructed from 2022 back to 2002 using guiding MODIS LAI and evaluated with in-situ data. The most consistent reconstructed product was FVC ($R = 0.96$, NRMSE $= 0.17$) over mixed forests compared to CGLS estimates. FVC also yielded the highest validation statistics ($R = 0.93$, $\rho = 0.92$, NRMSE $= 0.14$) over croplands. The highest correlation coefficients were achieved by the predictor variable LAI reconstructing FVC with mean R, ρ and NRMSE $= 0.11$ among all sites of 0.91 and 0.88, respectively. In the absence of both satellite and ground-based LCC reference measurements, the reconstructed LCC profiles were compared to the OLCI and MERIS Terrestrial Chlorophyll Index (OTCI, MTCI). The correlation metrics provided strong evidence of the reconstructed LCC product's integrity, with the highest correlation over deciduous broadleaf, mixed forests and croplands ($R > 0.9$). The lowest correlations for all reconstructed variables appeared over evergreen broadleaf forests, driven by the absence of seasonal patterns. Altogether, by leveraging the flexibility of the MOGPR algorithm with guiding historical data, contemporary EO data can be extrapolated into the past.

1. Introduction

Climate change poses ever greater pressure to understand and evaluate the multi-decadal evolution of ecosystems and biophysical processes (Luo et al., 2011). Earth-observing satellite missions facilitate and support global-scale monitoring of environmental dynamics and related land use changes (Winkler et al., 2021). Essential Climate Variables (ECVs) are physical, chemical, and biological variables, or a set of grouped variables, that play a crucial role in the Earth system's dynamics (Global Climate Observing System (GCOS), 2022). ECVs provide

empirical evidence to understand, monitor, and mitigate risks associated with Earth's climate (Zemp et al., 2021), but also biodiversity and other environmental changes. The importance of the global assessment of ECVs was recognized by the Global Climate Observing System (GCOS) and supported by the European Union's Earth Observation Programme, Copernicus (Thépaut et al., 2018). Among many, one of the services offered by Copernicus is the Climate Change Service (C3S), which provides extensive information encompassing various Earth-system components, including the atmosphere, land, ocean, sea-ice, and carbon. The C3S focuses on producing a consistent and comprehensive overview of the past, current, and future Earth climate via the generation of 20 ECVs (Buontempo et al., 2022). The environment's response to climate change is predominantly gathered from satellite observations leading to the retrieval of ECVs, constituting the principal source of information. However, with a few exceptions, most satellites do not provide multi-decadal imagery, either because of their short life cycle or recent launch dates (Fuchs et al., 2013; Joshi et al., 2016; Kooistra et al., 2023; Winkler et al., 2021). For instance, vegetation products (VPs) retrieved by Sentinel-3 Ocean and Land Colour Instrument (S3 OLCI) data have only been available since S3's launch in 2016, which limits evaluating long-term, multi-decadal time series of biophysical variables based on the same data stream. Apart from monitoring marine and coastal water qualities, one of the S3 mission's objectives is to assess land surface properties, such as vegetation cover, land use and land cover (LC) changes (De Grave et al., 2020; Jutz and Milagro-Pérez, 2020), which are crucial areas of research within the context of the Copernicus program in Europe. While data collected by sensors with coarse resolution, like the NOAA-Advanced Very High Resolution Radiometer (AVHRR) sensor launched in 1979, provides valuable long-term observations, it has limitations for monitoring fine-scale land cover changes in Europe. In contrast, medium-resolution imagery, such as those from the Moderate Resolution Imaging Spectrometer (MODIS), offers a promising compromise between LANDSAT/SPOT and AVHRR imagery since 2000 (Clevers et al., 2005; Mucher et al., 2000). The OLCI mission's land applications are tailored to maintain the continuity of MODIS and Medium Resolution Imaging Spectrometer (MERIS) sensors (Donlon et al., 2012). OLCI measures the spectral reflectance of the Earth's surface in 21 spectral bands, ranging from 400 to 1020 nm, with a spatial resolution of 300 m. Amidst numerous environmental variables, such as snow cover, and coastal chlorophyll concentration in oceans (Garnesson et al., 2021; Ghent et al., 2017; Nagler et al., 2018), key VPs can be retrieved by OLCI and mapped on global scales (Gobron et al., 2022; Kovács et al., 2023b). These VPs include two ECVs, namely the leaf area index (LAI) and the fraction of absorbed photosynthetically active radiation (FAPAR), and other important variables describing the Earth's surface and the vegetation physiological states, namely fractional vegetation cover (FVC), and leaf chlorophyll content (LCC). Moreover, these four VPs are considered key variables essential to the interpretation of sun-induced fluorescence within the S3-FLEX (FLuorescence EXplorer) tandem mission concept (De Grave et al., 2020; Drusch et al., 2017). These VPs can be briefly described as follows:

FAPAR quantifies the proportion of solar radiation within the 400–700 nm spectral domain that is absorbed by active vegetation, expressed as a ratio to the total surface incident radiation (Sellers et al., 1997). It is an important variable for the modelling of primary production (see review by (Weiss et al., 2004)). Additionally, FAPAR is an observational constraint for the simulation of atmospheric carbon fluxes in biosphere models (Kaminski et al., 2012; Knorr et al., 2010). FVC represents the proportion of vegetation visible from a nadir point of view and refers to the coverage of photosynthetic leaf areas (Deardorff, 1978). FVC serves as a crucial biophysical variable for modelling land surface dynamics, addressing climate change implications, and enhancing numerical weather prediction accuracy (Zeng et al., 2000). LAI is half of the collective leaf area intercepting sunlight per area of the surface (Chen and Black, 1992). This variable is strongly associated with evapotranspiration and canopy photosynthetic activity. LAI is also a key

element in biogeochemical ecosystem cycles (Bréda, 2003; Chen and Black, 1992; Weiss et al., 2004). The solar radiation that is absorbed by the leaves is controlled by the pigments that are responsible for photosynthetic activity, mainly chlorophyll *a* and b. LCC drives photosynthetic potential and contributes to primary production (Curran et al., 1990; Gitelson et al., 2003). FAPAR and LAI are part of the 55 ECVs (Baret et al., 2013; Bojinski et al., 2014). Together with FVC and LCC, these four VPs offer valuable insights into vegetation health and ecosystem integrity. Recognizing their collective importance, multi-decadal data records of such variables can provide traceable evidence for past, current, and possible future ecosystem variability (Bojinski et al., 2014).

Such multi-decadal monitoring of ECVs would help to learn about how the land cover has changed, e.g., due to climate-induced vegetation shifts (Linderman et al., 2010) or human-induced land transitions such as deforestation, afforestation, and expansion of cultivated areas (e.g., Barona et al., 2010; Cavalli et al., 2023; Winkler et al., 2021). The quantification of multi-decadal ECV monitoring would support the World Meteorological Organization's (WMO) recommendation for the calculation of climate normals of bio-geophysical variables for every 30-year period. The 30-year normals could be considered as representatives of current and predictors for future changes within the climate system. (Devasthale et al., 2023; Livezey et al., 2007).

For the analysis of temporal trends over multiple decades, one of the most important aspects of satellite data and derived products, e.g., VPs, is its consistency. Typically, a solution for obtaining multi-decadal time series relies on a sequence of multiple sensors, such as S3 followed back in time by MERIS or MODIS. Nonetheless, data from subsequent satellite missions are not equal in terms of radiometric accuracy and spatial resolution, among others, leading to biases and uncertainties in derived products (Chander et al., 2013). On top of that, VP products of different satellite data sources can further deviate due to differences in the implemented retrieval algorithm (e.g., Bayat et al., 2021; Xiao et al., 2016). This holds especially true in the current era of data-driven models, where not only the selected algorithm but also the critical role of the training data determines the retrieval (e.g., Berger et al., 2021; Elmes et al., 2020). All these factors combined make it especially challenging to use one-to-one sequences of a VP from multiple sensors to track trends over a longer period. A harmonization method is needed for consistent decadal product reconstruction across sequences of multi-sensor data streams, so supporting a reliable long-term record of VPs related to land use, climate change, land degradation (Dubovyk, 2017) and related environmental assessments (e.g., Fang et al., 2019; Muradyan et al., 2022; Pan et al., 2018).

Temporal reconstruction techniques serve to fill in gaps in satellite imagery caused by clouds or other factors (e.g., Pipia et al., 2022; Poggio et al., 2012; Vuolo et al., 2017). Throughout the scientific literature, numerous studies have presented temporal reconstruction techniques for satellite imagery, including cloud removal (i.e., gap-filling) (e.g., Belda et al., 2020; Caballero et al., 2023; Mateo-Sanchis et al., 2018; Tang et al., 2013; Xiao et al., 2015), and noise reduction (Moreno et al., 2014). Sensor malfunction or random error are also common issues that induce gaps in the data stream and need to be dealt with (Shen et al., 2015). In addition, data and sensor fusion methods prove to be an effective solution for the reconstruction of the missing data (Schmitt and Zhu, 2016). By their nature, these interpolation techniques are inapt for extrapolation, such as reconstructing products into the past beyond available observations. To adequately reconstruct past satellite data, auxiliary guiding data and, at the same time, powerful algorithms are needed to enable meaningful extrapolation. For instance, gradient-boosted decision trees, using land surface temperature (LST), reflectance and LC data streams as ancillary inputs, have been used to simulate long-term solar-induced fluorescence data (Chen et al., 2022). In another example, surface reflectance and the normalised difference vegetation index (NDVI) were successfully reconstructed by (Xiao et al., 2017) using NASA's land long-term data record (Pedelty et al., 2007).

The leverage of machine learning (ML) regression algorithms has become a preferred methodology in recent years for processing a plethora of remote sensing time series applications (e.g., Su et al., 2021; Xi et al., 2021; Xu et al., 2021). Gaussian process regression (GPR) emerged as a powerful ML method for non-parametric regression and function approximation. GPR has been successfully applied for bio-physical variable retrieval from optical imagery (e.g., Caballero et al., 2022; Estévez et al., 2022; Kovács et al., 2023b; Reyes-Muñoz et al., 2022; Verrelst et al., 2012a). These models not only provide predictions but also uncertainty estimates (e.g., García-Soria et al., 2024; Verrelst et al., 2012b, 2013). As a flexible ML prediction method, GPRs can be used for time series reconstruction and gap-filling purposes. By using a specifically designed covariance function, which is learned from the data, along with the associated mean and standard deviation (the model's prior knowledge), GPR can describe a probability distribution over functions (the model's posterior knowledge), shaping the model's predictions and uncertainties. (e.g., Amin et al., 2022; Pipia et al., 2021; Salinero-Delgado et al., 2021). For a comprehensive introduction to GPR models, refer to Rasmussen and Williams (2006) and to Camps-Valls et al. (2016). Based on GPR, an attractive opportunity for harmonized time series reconstruction based on multiple data sources is given by multi-output GPR (MOGPR) (Álvarez et al., 2012). The idea of multi-source learning originated from the field of geostatistics (Goovaerts and Goovaerts, 1997). The main difference between GPR and MOGPR is that GPR assumes that the model inputs are independent, adversely, MOGPR allows for the possibility of correlation between multiple inputs, exploring the relationships between them to model the MOGPR model outputs.

The MOGPR methodology can identify appropriate cross-covariance functions for the multiple outputs, enabling the representation of these outputs as a single GPR with a well-defined covariance function (Álvarez et al., 2012). In the context of Earth observation (EO) data streams, MOGPRs have been used to exploit the dependencies between distinct yet complementary data streams (e.g., optical with radar) (e.g., Caballero et al., 2023; Pipia et al., 2019). MOGPRs are effective in simultaneously modelling multiple outputs, enabling the transfer of valuable information across the inputs (Lin et al., 2021), thus allowing for the reconstruction of harmonized data streams through independent yet complementary data sources. The presented MOGPR algorithm is particularly ambitious as it exploits the complementary connection between two independent data streams, constructs a cross-domain kernel function capable of transferring information across time series, and executes reconstruction (Pipia et al., 2019). As such, with the guidance of one archived long-term data stream, this MOGPR multisensor fusion approach can ensure continuous (i.e., gap-free) harmonized data streams from both data sources, thus leading to a long-term backwards reconstructed product.

Overall, given the temporally limited data archive of currently operational missions such as S3, we identified a lack of reconstruction methods for the production of multi-decadal continuous ECV data streams based on guiding archived products. Hence, to realize such reconstructed long-term data streams, flexible time series extrapolation workflows need to be developed that enable robust and accurate multi-decadal data reconstruction. Moving along these lines, the objectives of this study are threefold. We aim to:

1) explore the MOGPR algorithm's fusion ability to model complex relationships between multi-decadal MODIS-based predictors and S3-based target VPs. Furthermore, we will investigate the temporal interactions between predictors and reconstructed VPs to provide a rationale for the LC-specific reconstruction accuracy;
2) analyze the impact of various MODIS predictor variables, namely FAPAR, LAI, and NDVI, on the consistency of reconstructed S3 vegetation products over the 2002–2022 temporal range; and,
3) evaluate how consistently the proposed workflow reconstructs multi-decadal FAPAR, LAI, FVC and LCC temporal profiles using S3 data

compared to satellite-based reference data streams and ground-based observations.

2. Materials and methods

The following key steps were implemented to reconstruct S3 OLCI-based products, as also depicted in the flowchart of Fig. 1. First, we provide the theoretical background of the MOGPR formulations (Section 2.1). Second, the two main vegetation products are described, i.e., those to reconstruct (long-term Sentinel-3 VPs, hereafter named S3-MOGPR) and those to use as predictor biophysical variables from MODIS, here named as preVars. As an example, the MODIS-based predictor LAI is hereafter referred to as "preLAI". Both the reconstructed S3-MOGPR and MODIS-based preVars datasets are described in Section 2.2. Nine GBOV sites across LC types were selected and site-specific, local MOGPR models were trained over the year 2019 (Global Vegetation Observations (GBOV), 2023; Brown et al., 2020). We tested our algorithm over specific regions of interest (ROI) described in Section 2.2.2. Statistical evaluation against benchmark and in-situ data of the reconstructed time series using hold-out correlation and validation is presented in Section 2.3. To represent the practical application of the algorithm, temporally reconstructed maps were produced showing the phenological patterns of different land covers. Two sites with 50 km radius region of interest were selected, namely the Central Plains Experimental range in Colorado, US and Hainich in Germany.

2.1. Theoretical background

2.1.1. Single-output Gaussian process regression

To acquire a thorough understanding of the foundational methodology upon which MOGPR is built, we first explore Single-Output Gaussian Process Regression.

Suppose $\mathscr{D} = \left\{ t_i, y_i \right\}_{i=1}^{N}$ is a set of N pairs of parameter y_i obtained at time t_i. These are used in order to learn a function f to predict parameter estimates of new t inputs. The equation to predict y_i is defined as:

$$y_i = f(t_i) + e_i, \quad e_i \sim \mathscr{N}\left(0, \sigma_n^2\right)$$

given that $t \in \mathbb{R}$, the variance is σ_n^2 and $f(t)$ is the prediction function, and $\mathscr{N}$ is the additive noise. If we define $\boldsymbol{t} = [t_1, ..., t_N]^{\mathsf{T}}$ the model shall calculate that $f(t)$ is normally distributed with a zero mean. Furthermore, the covariance matrix is formulated as $\boldsymbol{K}(t, t)$. Kernels, such as the Matern 3/2 kernel (Rasmussen and Williams, 2006), are used in order to relate the similarity between input t with the i, j calculated by the kernel function $k(t_i, t_j)$.

Given the training data as $p(f^*|\mathrm{D}, t^*)$, it allows for the estimation of the distribution of f_* at point t_*.

Thanks to the Bayesian nature of the GPR algorithm the mean and variance are given by:

$$f(t^*) = \mu_{\mathrm{GP}}(t^*) = \boldsymbol{k}^{\mathsf{T}}\left(\boldsymbol{K} + \sigma_n^2 \boldsymbol{I}_N\right)^{-1}\boldsymbol{y}$$
$$\sigma_f^2(t^*) = \sigma_{\mathrm{GP}}^2(t^*) = c - \boldsymbol{k}^{\mathsf{T}}\left(\boldsymbol{K} + \sigma_n^2 \boldsymbol{I}_N\right)^{-1}\boldsymbol{k}^*$$

in which, k is an N by 1 vector, $y = [y_1, ..., y_N]^{\mathsf{T}}$ and $c = k(t, t) + \sigma_n^2$ and $f(t_*)$. The hyperparameters are adjusted by the marginal likelihood maximization for the model (Rasmussen, 2004), cross-validating (Snee, 1977) or by Bayesian learning process (Love and Jones, 2012).

2.1.2. Multi-output Gaussian process regression

The use of Gaussian processes and probabilistic models for multi-output learning was pioneered in geostatistics, where prediction over vector-valued output data is known as cokriging (Journel and Huijbregts, 1978). Geostatistical approaches to multivariate modelling are often based on the Linear Model of Coregionalization (LMC) (Álvarez et al., 2012), which can be seen as a generative method for creating valid
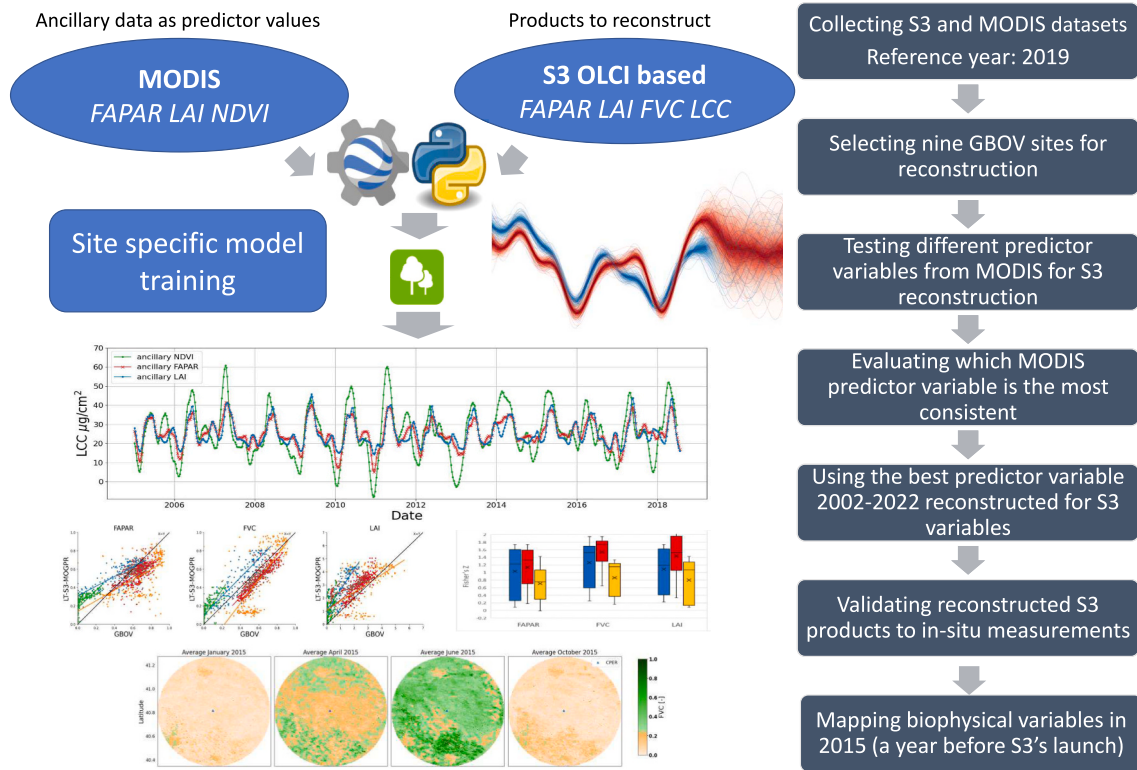
Fig. 1. Flowchart workflow followed throughout this study.

covariance functions. In the LMC, the outputs are represented as linear combinations of independent random functions. This is done in such a way that the resulting covariance function, expressed jointly over all the inputs and outputs, is a valid positive semidefinite function.

For the sake of simplicity, we will assume an isotopic model (Wackernagel, 2003) for the multi-output model analysis in all future discussions. This means that the model's observed data have been collected at the same point locations, and the frequency of the acquisitions is also the same. As a result, the model will have an equal amount of input data for modelling the cross-covariance between the model's outputs.

Consider a set of $\mathscr{D}$ correlated outputs $\{f_d(t)\}_{d=1}^{\mathscr{D}}$. Imagine that we have $\mathscr{C}$ groups of random processes with covariance functions $\{k_1(t,t'), k_2(t,t'), \ldots k_q(t,t')\}$, and for each group, we have obtained $\mathcal{R}_q$ samples independently from the same Gaussian process. Each element $f_d(t)$ is expressed as the linear combination of zero-mean latent functions $\{u_q^i(t)\}_{q=1}^{\mathscr{C}}$ and it can then be formulated as:

$$f_d(t) = \sum_{q=1}^{\mathscr{C}} \sum_{r=1}^{\mathcal{R}_q} a_{d,q}^i u_q^i(t), \quad d = 1, \ldots, \mathscr{D} \tag{1}$$

in which $a_{d,q}^i$ are the scalar coefficients corresponding to the $i-th$ sample of the latent Gaussian process, the d model's output, and the q group of input observed data. The $u_q^i(t)$ is the random sample of the Gaussian processes with covariance function $k_q(t,t') = cov\left[u_q^i(t), u_q^{i'}(t')\right]$. The processes $u_q^i(t)$ with $q = 1, \ldots, \mathscr{C}$ and $i = 1, \ldots, \mathcal{R}_q$, have the same covariance function.

Generalizing, for the multi-output case where $f(t) = [f_1(t) \ldots f_{\mathscr{D}}(t)]^T$, the covariance is given as:

$$cov[f(t), f(t')] = \sum_{q=1}^{\mathscr{C}} \boldsymbol{A}_q \boldsymbol{A}_q^T k_q(t,t') \tag{2}$$

where $\boldsymbol{A}_q = \left[a_q^1, a_q^2 \ldots a_q^{R_q}\right]$ is a matrix containing all the stacked scale parameters of the LMC model. We can then define a matrix $\boldsymbol{B}_q = \boldsymbol{A}_q \boldsymbol{A}_q^T$ commonly known as coregionalization matrix.

Assuming all outputs have the same number of training samples N, The methodology can be achieved by having different numbers of sources for each output function.

If $\boldsymbol{T}_d = [t_{1,d}, \ldots, t_{N,d}]^\top$ is a vector with the time samples of output d and $\mathbf{T}^\top = [\mathbf{T}_1^\top, \ldots, \mathbf{T}_{\mathscr{D}}^\top]^\top$ is a vector of all time samples, the LMC's full covariance matrix is formulated as:

$$\mathscr{K}(\mathbf{T}, \mathbf{T}) = \sum_{q=1}^{\mathscr{C}} \mathbf{B}_q \otimes \mathbf{K}_q(\mathbf{T}, \mathbf{T}) \tag{3}$$

in which $\otimes$ is the Kronecker product and $\mathbf{B}_q \in \mathbb{R}^{\mathscr{D} \times \mathscr{D}}$ are rank-$\mathcal{R}_q$ positive definite matrices. These principles form the foundation of the method as they summarize the connections between the various outputs.

Starting from a generative model for the outputs, the LMC leads to a sum of separable kernels. This sum represents the covariance function as the sum of the products of two covariance functions. The first covariance function (the coregionalization matrix $\boldsymbol{B}_q$) models the correlation between outputs. The second covariance function models the input dependence independently of the particular set of functions $f_d(t)$ (the covariance function $k_q(t,t')$).

Considering the MODIS–S3 fusing approach, the configuration parameters for the MOGPR model are $\mathscr{D} = 2$ (number of outputs), $\mathscr{C} = 2$ (number of different random processes), and $\mathcal{R}_q = 2$ (number of samples for each random process). Let $\mathfrak{D}_1 = \{(t_i, f_1(t_i)) | i = 1, \ldots, N\}$ be a set of N pairs of random functions f_i extracted from S3 OLCI data acquired at times t_i and $\mathfrak{D}_2 = \{(t_i, f_2(t_i)) | i = 1, \ldots, N\}$ the correspondent VPs samples derived from MODIS data, if f_1 and f_2 follow a Gaussian process, the formulation of the LMC presented in Eq. (1) can be interpreted as follows:

$$f_1(t) = a_{1,1}^1 u_1^1(t) + a_{1,1}^2 u_1^2(t) + a_{1,2}^1 u_2^1(t) + a_{1,2}^2 u_2^2(t)$$
$$f_2(t) = a_{2,1}^1 u_1^1(t) + a_{2,1}^2 u_1^2(t) + a_{2,2}^1 u_2^1(t) + a_{2,2}^2 u_2^2(t) \qquad (4)$$

Fig. 2 schematizes the MOGPR modelling for the S3 OLCI and MODIS Vps inputs reconstruction based on the LMC. Most conveniently, the MOGPR methodology is attained by modelling each channel as a single output Gaussian process. If the results show correlation, the single output approach neglects to consider the correlations among the model outputs, thereby compromising the consistency of regression processes (Bonilla et al., 2007). To consider the possible dependencies between the processes, we write the joint multivariate Gaussian distribution in its simplified form:

$$f \sim \mathcal{N}(0, \mathbf{K_{f,f}}) \qquad (5)$$

where $\mathbf{K_{f,f}} = \sum_{q=1}^{\ell} \mathbf{B}_q \otimes \mathbf{K}_q$ with $\mathbf{K}_q \in \mathbb{R}^{N \times N}$, describes the covariance for the joint process. With regard to the MODIS–S3 fusing approach, if we have a finite number of random variables for these independent processes (f_1 and f_2), they can be stacked to finally obtain the random vector-valued function. By creating a larger vector, the following is yielded:

$$\begin{bmatrix} f_1 \\ f_2 \end{bmatrix} = \begin{bmatrix} f_1(t_1) \\ \vdots \\ f_1(t_N) \\ f_2(t_1) \\ \vdots \\ f_2(t_N) \end{bmatrix} \sim \mathcal{N}\left(\begin{bmatrix} 0 \\ 0 \end{bmatrix}, \sum_{q=1}^{\ell} \mathbf{B}_q \otimes \mathbf{K}_q \right) \qquad (6)$$

For a detailed review and description of the methodology and also for an explanation regarding the multi-output prediction and uncertainty calculations for a given new input t_* value, consider the publications of (Álvarez et al., 2012; Caballero et al., 2023; Pipia et al., 2019). Throughout the presented workflow, the Python-based GPy library (GPy, 2012) was used, with the Matern 3/2 Covariance Kernel specification. For an in-depth explanation of the methodology, readers are advised to consider the work presented by Pipia et al. (2019). In practice, thanks to the covariance functions between the introduced multi-source data streams, e.g. given a historical data stream and a more limited data stream, the MOGPR fitting reconstructs harmonized multi-source data streams along the entire temporal window with a user-defined temporal sampling, e.g. every 8 days.

2.2. Vegetation products

2.2.1. Vegetation products used for long-term reconstruction

Throughout the analysis, we analyzed key VPs for, MOGPR model training, decadal reconstruction, correlation, and validation. The main satellite VPs included S3 OLCI-based FAPAR, FVC, LAI, and LCC for long-term reconstruction and MODIS-based FAPAR, LAI, and NDVI for predictor time series input to the MOGPR algorithm (see also Table 1). The four VPs that were reconstructed were inferred by using hybrid methods applied to S3 OLCI top-of-atmosphere (TOA) radiances on S3 scenes acquired from 1st January 2019 to 27th December 2019 (Total No of scenes: 44). Key development steps of the hybrid models consisted of simulating top-of-canopy (TOC) reflectance spectra with various leaf canopy states using the SCOPE model (v.1.7.) (Van Der Tol et al., 2009). Biochemical, biophysical, soil, and geometry variables were sampled to
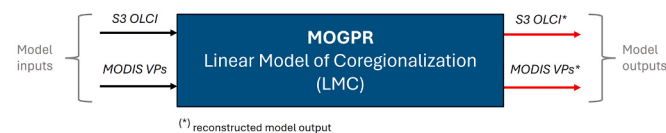

Fig. 2. Block diagram of MOGPR modelling based on the Linear Coregionalization Model (LMC).

execute SCOPE simulations. The input variable values, ranges, and distributions for the SCOPE and 6SV models, as applied in our study, are described more in detail by De Grave et al. (2020); Reyes-Muñoz et al. (2022). In addition, TOA radiance spectra of non-vegetated surfaces from S3 imagery were selected (e.g., water, soil, and rocks) to complement training input for mapping of heterogeneous surfaces (Kovács et al., 2023b; Reyes-Muñoz et al., 2022). These simulations were coupled with the 6SV radiative transfer model (RTM) (Kotchenova et al., 2006; Vermote et al., 1997) to enable biophysical variable retrieval directly from TOA radiance data. For the detailed atmospheric properties used throughout the simulation, readers are advised to consult Table 2 from Kovács et al. (2023b). GPR algorithms were then trained on the TOA simulations, learning the nonlinear relationship between reflectance and variables. Note hereby, since the SCOPE-simulated canopies were a function of green leaves only, thus strictly speaking, the retrieved canopy variables LAI and FVC refer to green LAI, green FVC, while FAPAR refers to green instantaneous FAPAR of the leaves. For a thorough explanation of the biochemical leaf and canopy structure variables used for simulations, readers are referred to Table 1 in Reyes-Muñoz et al. (2022). Also, to evaluate the validity of the GPR models at the continental and global scale, FAPAR, FVC, LAI, and LCC data streams were earlier adequately validated (Reyes-Muñoz et al., 2022), and successfully inter-compared against reference MODIS and CGLS-based EO products for the entire year 2019 (Kovács et al., 2023b). These maps can also be retrieved by the PyEOGPR package (D.Kovács, 2024).

To train the MOGPR models for reconstruction, a comprehensive dataset encompassing predictor variables from MODIS (FAPAR, LAI, and NDVI (Myneni et al., 2015)) and target variables from S3 (FAPAR, FVC, LAI, and, LCC), composited into an 8-day temporal resolution, was compiled for the year 2019. Each of the satellite products has been resampled to MODIS' VPs nominal resolution, 500 m pixels, to adequately match target (S3) and predictor (MODIS) spatial footprints. The vegetation products were handled in GEE with the Python API (Google Earth Engine, 2023). The used products and their descriptions are given in Table 1. For each time step, the average of the coinciding pixels within the sites was taken in a square (1.5 km × 1.5 km). This square enabled the comprehensive assessment by aggregating pixels since all datasets can have gaps and inconsistencies when only focusing on a single pixel. Additionally, the square region covered the entire footprint of the upscaled in-situ reference measurements, as thoroughly described by (Global Vegetation Observations (GBOV), 2023; Brown et al., 2020). The S3-MOGPR data was finally obtained for each S3-based VP using MODIS FAPAR, LAI, and NDVI as input to the MOGPR temporal reconstruction algorithm for the years between 2002 and 2022.

2.2.2. Reference vegetation products and sites

Table 2 lists the satellite and ground-based datasets used for both correlation and validation. For each reconstructed S3-MOGPR variable (i.e., FAPAR, FVC, LAI, and LCC), three different time series were generated by using three different guiding predictor variables (i.e. pre-FAPAR, preLAI, and preNDVI). Each of these different reconstructed FAPAR-, FVC-, LAI-MOGPR profiles were correlated to data from the Copernicus Global Land Service (CGLS) originating the synergy PROBA-V, SPOT/VEGETATION and Sentinel-3 (Fuster et al., 2020). These products were downloaded from https://land.copernicus.eu/global/themes/vegetation (accessed on 11 November 2023). Table 2 summarizes the satellite and ground-based datasets used for both correlation and validation.

Due to the generally scarce availability of satellite-based LCC products, we relied on the MERIS and S3-OLCI Terrestrial Chlorophyll Index (MTCI and OTCI) as a reference measurements (Dash and Curran, 2007; Pastor-Guzman et al., 2020). Since both of these indices are surrogates of canopy chlorophyll content (CCC) the reconstructed LCC profiles were upscaled to CCC, by multiplying LCC with LAI:

$$CCC = LCC^* LAI \qquad (7)$$

Table 1

Satellite-based vegetation products that were reconstructed and used as predictor variable for reconstruction.

Usage	Product name	Vegetation product	Spatial-temporal resolution	Temporal availability	Retrieval method
Reconstructed variables	S3-MOGPR	FAPAR, FVC LAI, LCC	300 m - <4 days	2016 October -	Hybrid (GPR-SCOPE) (Kovács et al., 2023b; Reyes-Muñoz et al., 2022)
Predictor variables	MCD15A3H MODIS	FAPAR, LAI	500 m - 4 days	2002 July -	Principal algorithm using 3D RTM generated Look-up-Table based retrieval with red and NIR bands (Knyazikhin et al., 1998; Myneni et al., 2015)
	MOD09GA_006 MODIS	NDVI	500 m - daily	2002 February -	Normalised difference of near-infrared and red bands. Calculated with surface reflectances corrected for atmospheric conditions such as gasses, aerosols, and Rayleigh scattering (Vermote and Wolfe, 2021)

Table 2

Satellite and land-based vegetation products that were used for intercomparison.

Usage	Product	Vegetation Product	Spatial-temporal resolution	Temporal availability	Retrieval method	Reference
Correlation	Copernicus Global Land Service S3/PROBA-V/SPOT	FAPAR, FVC LAI	300 m - <4 days	1999–2020 June	Neural networks trained with reflectance data	(Verger and Adrià, 2022)
	OLCI Terrestrial Chlorophyll Index	OTCI	300 m - <4 days	2016 October to present	Computed from red, red-edge and NIR bands	(Pastor-Guzman et al., 2020)
	MERIS Terrestrial Chlorophyll Index	MTCI	1 km - 10 days	2005–2012	Computed from red, red-edge and NIR bands	(Dash and Curran, 2007)
Validation	Ground Based Observation for Validation (GBOV)	FAPAR (FIPAR), FVC LAI (PAI)	300 m (upscaled reference measurement) < weekly	2014–2022 (Site and Variable dependent)	Upscaled In-situ reference measurements with Sentinel-2 and Landsat 8 data	(Global Vegetation Observations (GBOV), 2023; Brown et al., 2020)

CCC profiles were compared to both MTCI and OTCI to achieve a more comprehensive evaluation of the reconstructed datasets. The reflectance spectra of vegetation exhibit lower values in the visible spectrum (400–700 nm) attributed to chlorophyll absorption, while NIR reflectance (700–1300 nm) is higher due to the internal leaf structure scattering (Horler et al., 1983; Pastor-Guzman et al., 2020). These interactions give rise to a red edge between 650 and 750 nm, which shifts to longer wavelengths at increased chlorophyll content (Brown et al., 2019a). The use of the red edge region for chlorophyll detection was first exploited with the Medium Resolution Imaging Spectrometer (MERIS). Its product, the MERIS Terrestrial Chlorophyll Index (MTCI) was developed to use the information in the red edge region to assess chlorophyll in plants. The continuity of this index is secured by its S3 successor, OTCI (Pastor-Guzman et al., 2020). The MTCI and OTCI indices are calculated as follows for the corresponding sensors, MERIS and OLCI:

$$MTCI = \frac{R_{10} - R_9}{R_9 + R_8} = \frac{R_{753.75} - R_{708.75}}{R_{708.75} + R_{681.25}} \tag{8}$$

$$OTCI = \frac{R_{12} - R_{11}}{R_{11} + R_{10}} = \frac{R_{753.75} - R_{708.75}}{R_{708.75} + R_{681.25}} \tag{9}$$

Since each MODIS preVar yielded a slightly different time series for each S3 target variable, due to the underlying interconnection between vegetation properties, the preVar whose reconstruction consistency was the highest, is selected to reconstruct S3-MOGPR vegetation products to be validated with in-situ reference measurements. To be able to compare biophysical variables (LCC and CCC) to MTCI and OTCI, these were normalised based on their seasonal minima and maxima. Note that the available MTCI data are provided at 10-day intervals, whereas OTCI data are available at 2-to-3-day revisit times (Donlon et al., 2012; UK Multi-Mission Product Archive Facility Infoterra Ltd et al., 2019).

2.2.3. GBOV reference measurements

To validate, upscaled reference measurements from the GBOV sites were used https://gbov.land.copernicus.eu/ (accessed on 12th December 2023). GBOV collects and unites data across various international research networks. To facilitate practical usage of the in-situ measurements, these were upscaled to represent larger areas enough to cover several pixels of mid-resolution satellites, such as S3 or MODIS. In-situ reference measurements were upscaled with the Sentinel-2 Level 2 Prototype Processor (SL2P). SL2P adopts artificial neural networks (ANNs) that are trained with RTM simulations from the coupled Leaf Optical Properties Spectra (PROSPECT) and Scattering by Arbitrarily Inclined Leaves (4SAIL) (Verhoef and Bach, 2007). SL2P used reflectances from Landsat-8 Operational Land Imager (OLI) and Sentinel-2 Multi Spectral Instrument at 20 m resolution, to generate upscaled reference measurements local bias corrected to the ground truth data (Brown et al., 2021).

Since GBOV is intended to be the official validation service for CGLS, it features FAPAR, FVC, and LAI in its catalogue of vegetation products, regrettably missing LCC (Bai et al., 2019). LAI reference measurements provided by GBOV are not accounting for foliage clumping (Fernandes and Djamai, 2019), thus the provided values refer to plant area index (PAI) as opposed to LAI, because the upwards-facing image classification is not able to distinguish between foliage and woody material. Moreover, GBOV-provided FAPAR values are actually fractional intercepted photosynthetic radiation (FIPAR) metrics as the vegetation is assumed to be completely absorbing when in reality some reflectance/transmittance occurs (Brown et al., 2021).

The S3-MOGPR was prototyped on a variety of LCs, both in the Northern and Southern Hemispheres. The location of the sites and information regarding their dominant LCs are depicted in Fig. 3 and Table 3. These specific sites were selected due to the availability of in-situ reference measurements for FAPAR, FVC, and LAI, so the long-term products could be validated. Moreover, the selection was also influenced by the need to investigate sites on various continents and different biomes. To showcase a practical application of the MOGPR temporal reconstruction algorithm, the four reconstructed biophysical variables were mapped over a circular region centered at one of the GBOV sites, i.e., the Central Plains Experimental Range (CPER) site, with a 50 km radius. These maps were produced throughout the year 2015, a year before S3's launch. To demonstrate the mapping applicability of MOGPR, Fig. 13 portrays maps of FVC, FAPAR, LAI, and LCC maps reconstructed throughout 2015 at 8 days temporal resolution, with monthly averages shown for four months. Satellite imagery in the visible
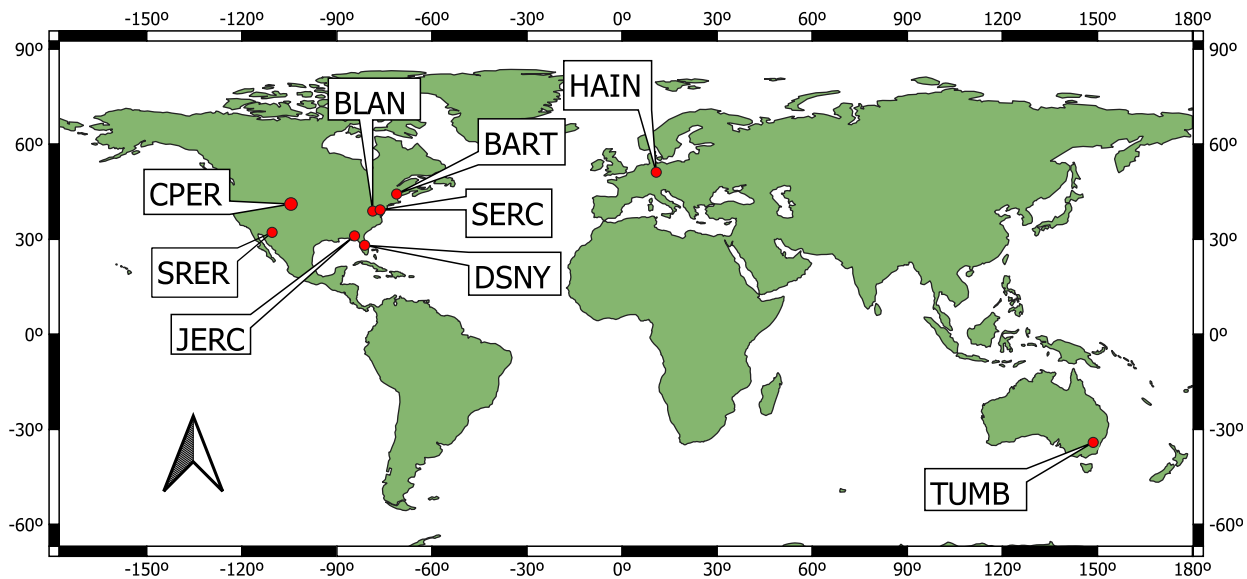
Fig. 3. Global map showing the locations of the nine GBOV sites, where S3-MOGPR products were reconstructed.

Table 3
GBOV validation sites used for long-term reconstruction of S3-MOGPR time series.

GBOV site name	Site abbreviation	Dominant LC (1.5 × 1.5 km)	Temporal window used for validation	Latitude (°)	Longitude (°)
Blandy Experimental Farm	BLAN	Deciduous Broadleaf	2016–2020	39.060	−78.716
Bartlett Experimental Forest	BART	Mixed Forest	2014–2020	44.064	−71.287
Central Plains Experimental Range	CPER	Grassland	2014–2020	40.816	−104.745
Disney Wilderness Preserve	DSNY	Open Shrublands	2014–2020	28.125	−81.436
Jones Ecological Research Center	JERC	Evergreen Needleleaf	2014–2020	31.195	−84.468
Smithsonian Environmental Research Center	SERC	Croplands	2015–2020	38.890	−76.560
Santa Rita	SRER	Shrublands	2016–2020	31.911	−110.835
Tumbarumba	TUMB	Evergreen Broadleaf	2020	−35.657	148.151
Hainich	HAIN	Mixed Forest	2020–2022	51.079	10.452

spectral domains and a representative LC classification map from the ESA GlobCover catalogue for the investigated area are shown Buchhorn et al. (2020). The site CPER was selected to represent MOGPR maps, due to the variety of LCs the circular area entails. These maps provide a practical application for the MOGPR temporal reconstruction algorithm. The selected four months (January, April, June, and October) were selected for representation due to their distinct growing stages of vegetation and they were mapped at 500 m resolution. The presented maps were processed through the openEO API and Terrascope back end (Schramm et al., 2021).

2.3. Statistical analysis and error metrics

The consistency of the S3-MOGPR products was assessed by correlating all reconstructed variables with their corresponding reference products, as outlined in Section 2.2. Additionally, FAPAR, FVC and LAI reconstructed variables were validated to in-situ reference measurements from the GBOV network (Global Vegetation Observations (GBOV), 2023; Brown et al., 2020).

For the statistical evaluation of the consistency of S3-MOGPR products against reference measurements, we used Pearson's (R) and Spearman's (ρ) correlation coefficients. Using 1.5 × 1.5 km match ups reduces measurement differences due to differences in the Projected Instantaneous Field of View of Measurement (PIFOV) of single OLCI and MODIS 500 m resolution inputs. Being a measure of the monotonic correlation, ρ has the advantage of avoiding skewed correlations, whereas R is highly sensitive to extreme outliers (Rodgers and Nicewander, 1988; Spearman, 1961). Additionally, in case of non-normality,

the implementation of Spearman's rho, as a non-parametric, rank-based alternative to Pearson's R is essential (Fowler, 1987; Khamis, 2008; Schober et al., 2018). Thus, it is advantageous to investigate both R and ρ to have a comprehensive understanding of statistical correlation and evaluation.

Additionally, to evaluate the error metrics between reconstructed and reference datasets, both root mean squared error (RMSE) and mean absolute error (MAE) in their normalised forms by their range (i.e., NRMSE and NMAE) were calculated. The difference between NRMSE and NMAE indicators is useful to assess the effect of outliers between the compared datasets. This could be expected as the errors increase in a quadratic manner, heavily penalizing the outliers for NRMSE. In cases where NRMSE is larger than NMAE, it indicates outliers in the compared datasets, that heavily penalize NRMSE. The calculation of these measures is formulated below in Eqs. (13) and (14). Moreover, to follow good practices of validation of the VPs and to make understanding easier how well the reconstructed data meet user requirements, bias, precision and user agreement rates (UAR) were also reported (Brown et al., 2020; Fernandes et al., 2014). These metrics are shown in Eqs. (10) and (11). The UAR is defined as the number of observations falling into the uncertainty user requirement for the ECVs (0.5 for LAI and 0.05 for FAPAR (Global Climate Observing System (GCOS), 2022)).

$$Bias = \frac{1}{N} \sum_{i=1}^{N} (X_i - Y_i) \qquad (10)$$

$$Precision = \sqrt{\frac{1}{N}\sum_{i=1}^{N}(X_i - Y_i) - Bias} \qquad (11)$$

$$NMAE(\%) = \frac{1}{n}\sum_{i=1}^{n}\frac{|X_i - Y_i|}{(Y_{max} - Y_{min})} \qquad (14)$$

$$RMSE = \sqrt{\frac{\frac{1}{N}\sum_{i=1}^{N}(X_i - Y_i)^2}{N}} \qquad (12)$$

$$NRMSE = RMSE \bigg/ \frac{\sum_{i=1}^{N}Y_i}{N} \qquad (13)$$

where X_i, Y_i are the individual values of estimated (X) and reference (Y) variables.

To assess the distinct correlation metrics of the reconstructed time series by different predictor variables, the mean of Pearson's R and Spearman's ρ were calculated, following the methodology described by (Fisher, 1915). Taking the regular arithmetic mean of correlation coefficients tends to result in underestimation due to the skewed nature of
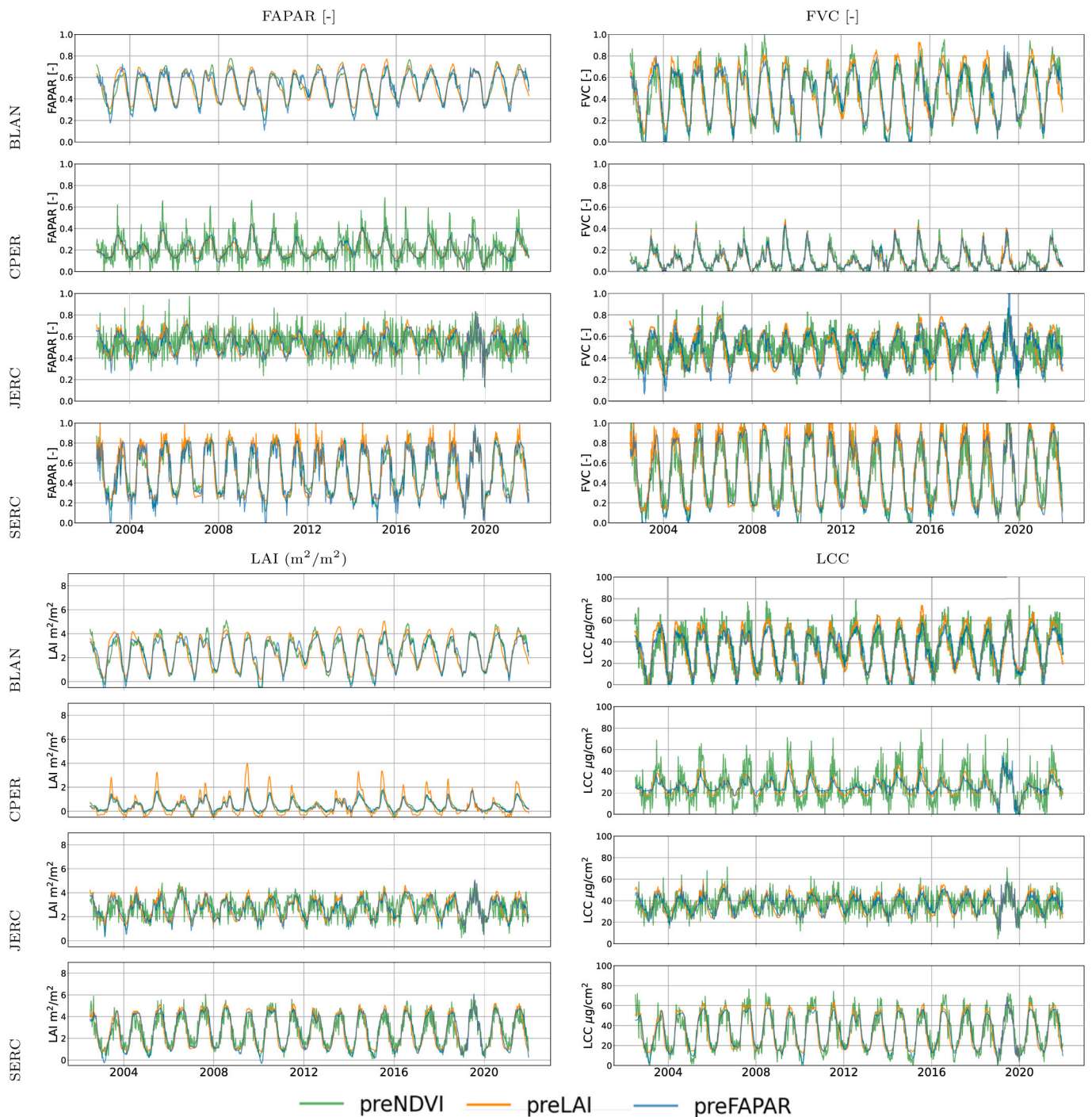
Fig. 4. Time series of S3-MOGPR FAPAR, FVC, LAI and LCC at BLAN, CPER, JERC, and SERC sites, reconstructed by each of the three predictor variables (preNDVI, preLAI and preFAPAR). Results of investigated temporal profiles at other sites are portrayed in Appendix A.

the sampling distribution (Silver and Dunlap, 1987). Evaluating the mean of correlation coefficients required the transformation of both R and ρ to Fisher's Z, which is formulated in Eq. (15):

$$Z = \frac{1}{2}ln\left(\frac{1+r}{1-r}\right) \tag{15}$$

where Z is the Fisher transformed sample correlation coefficient R or ρ, and r is the original correlation coefficient. It is a normalised version of the correlation coefficient, less affected by the skew of the sampling distribution (Corey et al., 1998). The depicted equation is essentially the correlation coefficient's inverse hyperbolic tangent function. The mean of various Fisher Z was calculated for both R and ρ, and the inverse function, Eq. (16) was used to obtain the average of the correlation coefficients ($\overline{R}$ and $\overline{\rho}$).

$$r = \frac{e^{2z} - 1}{e^{2z} + 1} \tag{16}$$

3. Results

To identify the most robust preVar for reconstruction, this section is divided as follows: Section 3.1 presents the resulting S3-MOGPR time series by the three preVars. The effect of the preVars is evaluated when correlating to satellite measurements in Section 3.2. The S3-MOGPR time series and their associated uncertainty are depicted within the 2002–2022 window reconstructed by the most effective preVar, along with the satellite and ground-based measurements in Section 3.4. The LCC-to-OTCI correlation is assessed in Section 3.3. To evaluate the accuracy of the reconstructed S3-MOGPR products, they were validated with in-situ reference measurements; see Section 3.6.

3.1. S3-MOGPR reconstruction by distinct predictor variables

Fig. 4 presents reconstructed time series data streams of all S3-MOGPR variables generated by the three guiding preVars. To facilitate visual comprehension of the temporal profiles, four selected sites are depicted in the main body of the paper (Fig. 4); the others are given in Appendix A. As expected, the reconstructed data streams vary depending on the site and the preVars used in the MOGPR fusion algorithm. Sites with LCs that show enhanced seasonality and greater cyclic patterns were better captured by all three predictor variables than those with lower yearly phenological dynamics. For LCs with pronounced seasonality, our S3-MOGPR outputs exhibited consistency, capturing yearly minima and maxima with similar amplitudes, despite variations in noise levels. This includes sites with LCs such as deciduous (BLAN) and mixed forests (BART and HAIN in Appendix A), and grasslands (CPER), all showing relatively similar time series generated by each of the three preVars.

Generally, preLAI-based reconstruction yielded the time series with the fewest fluctuations in amplitude. Both preFAPAR and preNDVI-

guiding output temporal profiles possess more noise in the time domain; however, the effect of these two preVars yields greater amplitude for the reconstructed time series in some cases. This effect for preFAPAR and preNDVI is especially apparent in the cases of preNDVI-FAPAR-MOGPR over grasslands (CPER), preNDVI-FVC-MOGPR over deciduous broadleaf forests (BLAN), and preNDVI-LCC-MOGPR over grasslands (CPER). When assessing the reconstruction outcomes of open and closed shrublands (DSNY, SRER in Appendix A) and evergreen broadleaf forests (TUMB in Appendix A), all depict radically different time series by the three preVars, with different amplitude, noise and phase.

3.2. Correlation of reconstructed S3-MOGPR products against satellite products

The reconstructed FAPAR-, FVC-, and LAI-MOGPR data streams were subsequently correlated to CGLS products, over the temporal window of 2002–2019. The statistical metrics, including correlation coefficients (R and ρ) with the error metrics (NRMSE and NMAE) normalised among different units to ensure equivalent parameters in the comparison, are given in Table 5. The results show a high correlation for the majority of the sites that have LCs with defined yearly seasonality (see: Fig. 4 and Table 3). The heatmaps (see Fig. 5) reveal that the reconstruction worked with efficiently over sites such as BLAN, BART, JERC, CPER, SERC, and HAIN, where both R and ρ present coefficients above 0.9. For the reconstructed FAPAR, FVC, and LAI, with a slightly lower performance when reconstructing FAPAR by preNDVI, showing R and $\rho < 0.8$. The accuracy of reconstruction over the shrublands of DSNY and SRER is governed by the used predictor variable. When comparing the correlation between preFAPAR and preNDVI over these sites, reconstruction heavily underperformed as opposed to using preLAI. As described in Section 3.1, preVars that propagated substantial noise and wider amplitudes to S3-MOGPR profiles, the NRMSE errors are substantially larger than NMAE for this predictor, especially apparent for mixed forests (see BART, HAIN in Appendix A).

Notable differences between Pearson (R) and Spearman (ρ) correlations were noted in the mixed forests of BART. For all reconstructed variables, by all predictors, R values were larger (~ 0.1–0.2) than for ρ. This indicates that the reconstructed temporal profiles show a greater linear relationship rather than monotonic trends toward CGLS reference data streams.

The grouped boxplots on Fig. 6 show the Fisher Z transformed correlation coefficients' and errors' spread, grouped by each preVar. The boxplots show that for all reconstruction cases, the highest mean Fisher Z metrics were obtained by preLAI, which also yielded the lowest spread. PreFAPAR, although with greater spread, displayed higher mean Fisher Z values when compared to preNDVI. The lowest error metrics were noted for LAI-MOGPR, where all predictors showed errors lower than 0.15, also with rather low variability compared to other S3-MOGPR variables. The average correlation coefficients were calculated using the

Table 5
Statistical metrics for comparing CCC to MTCI (2010–11) and OTCI (2020–21). CCC was attained by multiplying LCC by LAI values for the corresponding dates. Note, that TUMB does not feature available MTCI retrievals within the 2010–11 timeframe.

| CCC	OTCI						MTCI					
	R	rho	Bias	N	Precision	NRMSE	R	rho	Bias	N	Precision	NRMSE
BLAN	0.94	0.91	0.04	370	0.2	0.2	0.65	0.7	−0.04	58	0.2	0.2
BART	0.93	0.72	−0.09	354	0.17	0.19	0.95	0.67	−0.15	63	0.19	0.24
CPER	0.37	0.23	−0.25	298	0.06	0.25	0.71	0.71	−0.19	49	0.05	0.19
DSNY	0.63	0.6	0.01	365	0.11	0.11	0.81	0.82	0	63	0.13	0.13
JERC	0.77	0.76	0.01	182	0.16	0.16	0.94	0.9	−0.03	63	0.13	0.13
SERC	0.9	0.89	0.1	129	0.27	0.29	0.97	0.93	0.05	57	0.22	0.23
SRER	0.61	0.52	−0.2	289	0.03	0.21	0.52	0.71	−0.21	62	0.03	0.21
TUMB	−0.37	−0.24	−0.07	366	0.09	0.12	–	–	–	–	–	–
HAIN	0.79	0.77	−0.03	237	0.25	0.25	0.95	0.95	−0.03	51	0.14	0.14
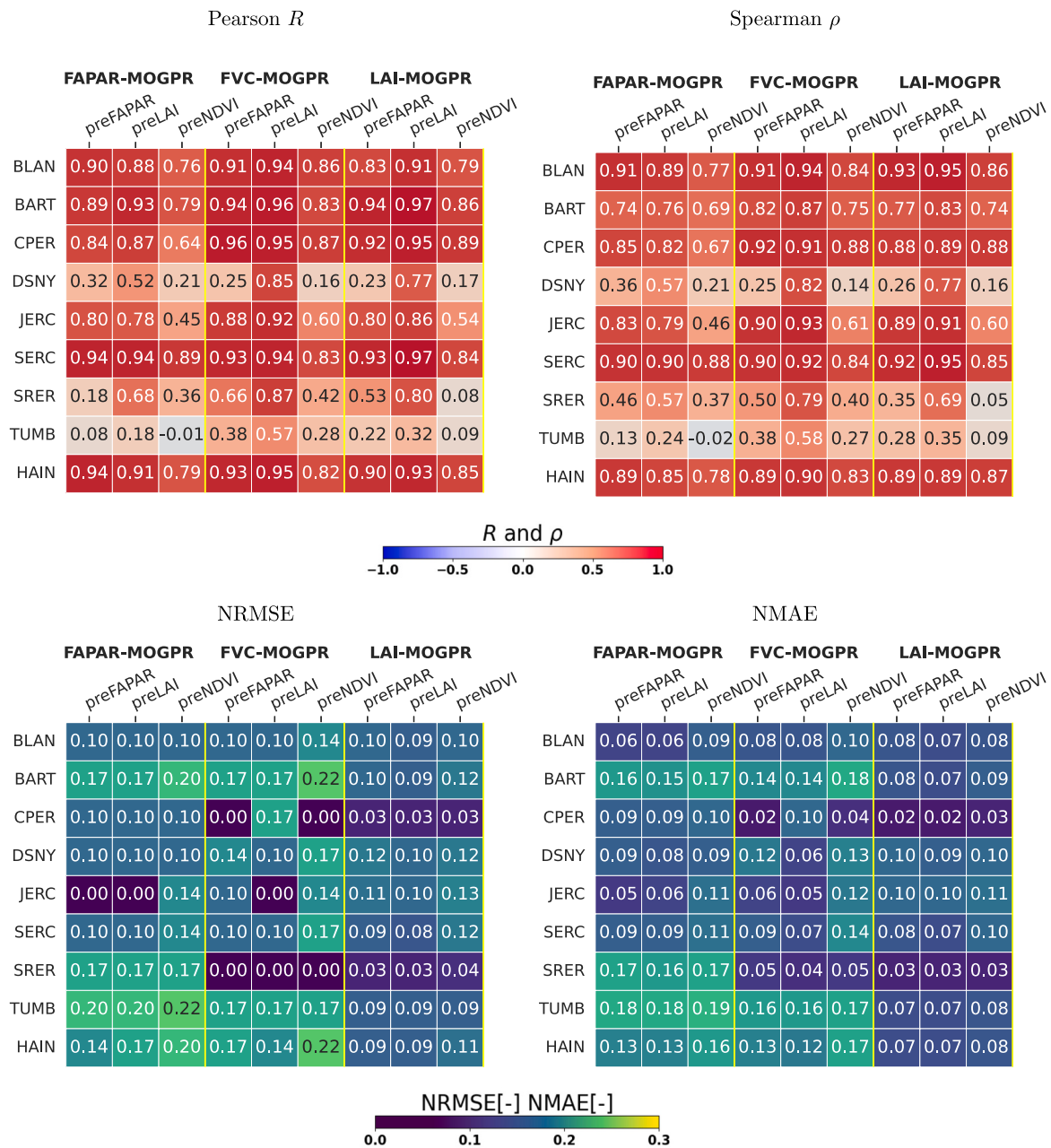
Fig. 5. Pearson, Spearman coefficients and normalised error metrics for correlating FAPAR, LAI and FVC-MOGPR to CGLS data from 2002 to 2019. The assessment of results by both R, ρ yields a comprehensive analysis of the monotonic and linear correlation between datasets.
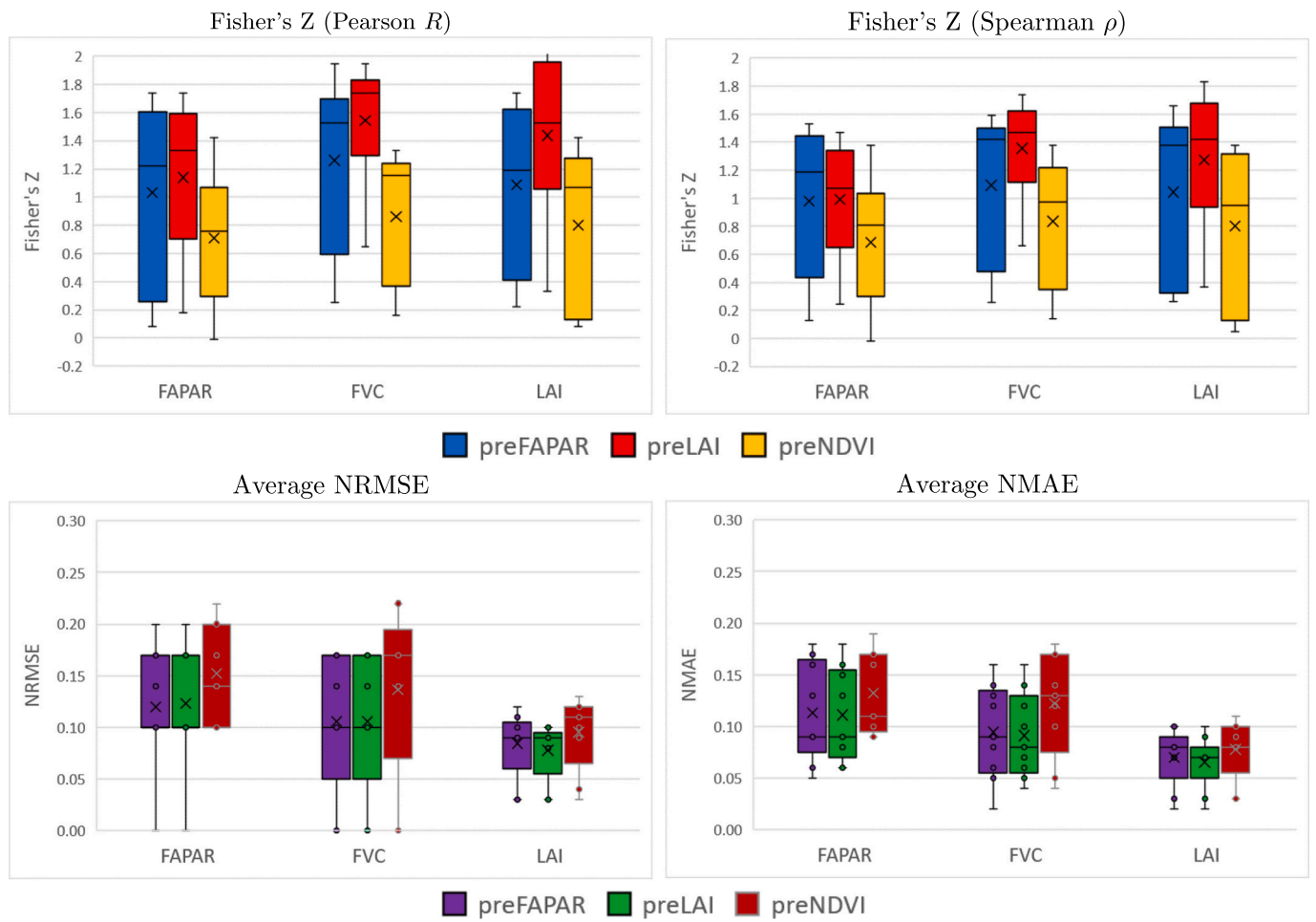
Fig. 6. Boxplots for the distributions of the Pearson (*R*) and Spearman (*ρ*) correlation coefficients Fisher's Z transformed form for FAPAR, FVC, LAI-MOGPR against CGLS data. Normalised error metrics (NRMSE, NMAE) are shown for the reconstructed S3-MOGPR variables' correlation. To facilitate an adequate comparison between coefficients, these boxplots display the Fisher Z transformed coefficients. × marks the mean, whereas the horizontal line in the boxes refers to the median.

Fisher Z transformation method, as described in Section 2.3, their average was calculated, and finally the inverse Fisher Z transform was applied to assess the averaged values. The best reconstruction method was using the MODIS LAI as predictor input. The averaged R, ρ is the highest for all S3-MOGPR variables when using preLAI, with the best performing case of FVC-MOGPR ($\overline{R}, \overline{\rho} = 0.91, 0.88$) followed by LAI-MOGPR ($\overline{R}, \overline{\rho} = 0.89, 0.85$) and FAPAR-MOGPR ($\overline{R}, \overline{\rho} = 0.81, 0.76$), as also shown in Table A.8. PreLAI and preFAPAR produced rather similar overall NRMSE and NMAE error metrics, but preLAI outperformed preFAPAR when considering correlation statistics (both R, ρ). The most effective way thus is to reconstruct by MODIS-based preLAI, then preFAPAR, and finally using preNDVI.

3.3. LCC statistical evaluation

Since the CGLS catalogue vegetation product range does not feature available LCC reference products, our LCC-MOGPR products were correlated to OTCI and MTCI. Since LCC, OTCI and MTCI have their own units, both were normalised to range between 0 and 1. The years 2020 and 2021 were used for correlation analysis. Table 7 shows correlation and error metrics comparing different temporal profiles of LCC-MOGPR obtained by using different preVars, correlating to OTCI. Generally, the reconstructed LCC profiles demonstrated consistency with the reference OTCI products, yielding high correlation metrics. (R and $\rho > 0.8$) over deciduous and mixed forests (BLAN, BART), JERC, SERC, and HAIN, when reconstructing with preLAI. When comparing LCC to MTCI, the most robust reconstructions were attained over BART, JERC, SERC and HAIN, all possessing pronounced intra-annual seasonality. Normalised error values stayed below 0.2 for these sites, both for NRMSE and NMAE. CPER and SRER exhibited inferior results, with R and ρ ranging between 0.5 and 0.7 with preLAI but showed metrics with lower agreements when reconstructed with the other two preVars. TUMB showed negative

correlations for all preVar cases, with higher error metrics (NRMSE > 0.3 and NMAE > 0.28) for all preVars. For numerical data regarding correlation and error metrics, see the preLAI column in Table 7. Despite the dissimilarities between the very nature of the two compared metrics, being a biochemical product (i.e., LCC) and a spectral index (i.e., OTCI and MTCI), the reconstructed data show moderately accurate results when MODIS-based preLAI is used, with the caveat of negative correlations over TUMB. The usage of preFAPAR and preNDVI as predictor inputs resulted in less effective reconstruction of LCC data streams.

The summarized, averaged correlation and error metrics, using the Fisher-Z method as explained in Section 2.3, are shown in Fig. 8. Similar to FAPAR, FVC, and LAI, for the LCC-OTCI comparison, the most consistent metrics were attained by using preLAI as a predictor, depicting the highest mean Fisher Z, lowest variability, and lowest error metrics. After using the inverse Fisher transform, the highest metrics were achieved for preLAI ($\overline{R}, \overline{\rho} = 0.78, 0.75$), followed by preFAPAR ($\overline{R}, \overline{\rho} = 0.56, 0.57$) and preNDVI ($\overline{R}, \overline{\rho} = 0.45, 0.44$). The scatter plots depicted between LCC and OTCI datasets in Fig. 9 show the values of LCC-MOGPR by preLAI and OTCI. LCC-MOGPR generally shows good agreement, with site-dependent biases. LCC-MOGPR over the shrublands (SRER) is overestimated, whereas the mixed forests (BART, HAIN) are slightly underestimated through end-of-season compared to OTCI. Evergreen broadleaf forest (TUMB) is negatively correlated.

Reconstructed LCC and CCC profiles behaved similarly to MTCI and OTCI with notable differences over BLAN, where LCC/CCC showed $R \sim$ 0.9 for OTCI, but only $R \sim 0.6$ for MTCI (see Table 4). Due to the fact that the investigated indices (OTCI and MTCI) are surrogates for canopy scale chlorophyll contents (CCC), LAI was multiplied by LCC to obtain CCC, and thus it could also be compared against the reference data (Dash and Curran, 2007; Pastor-Guzman et al., 2020). Note that some cases, where LAI is lower than 1, results in CCC showing values lower than LCC. The correlation metrics slightly improved by the upscaling,
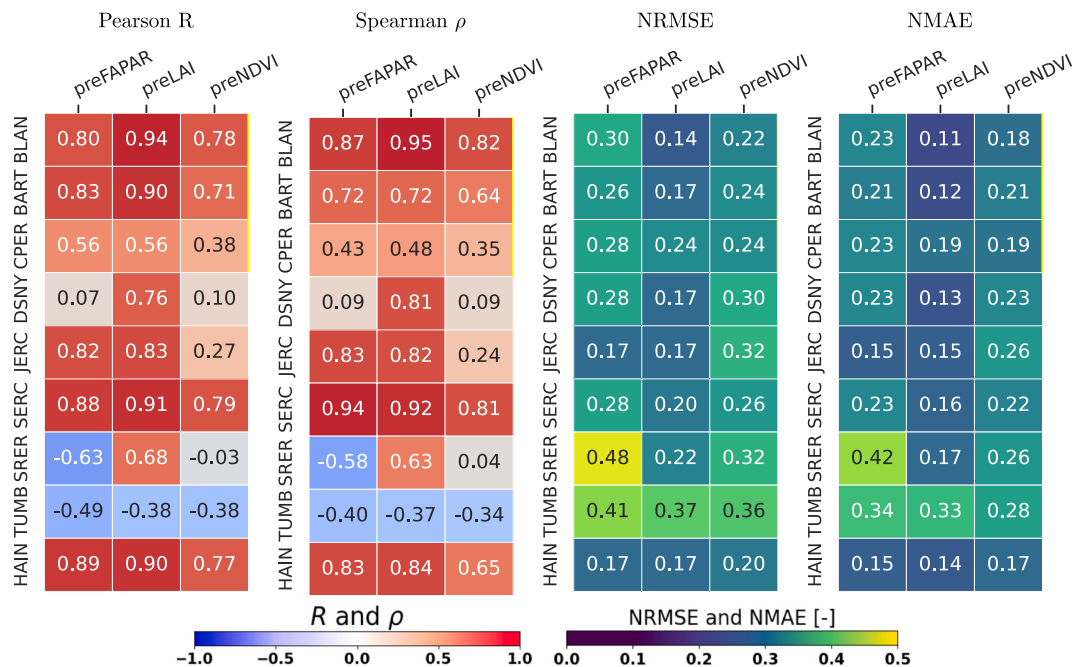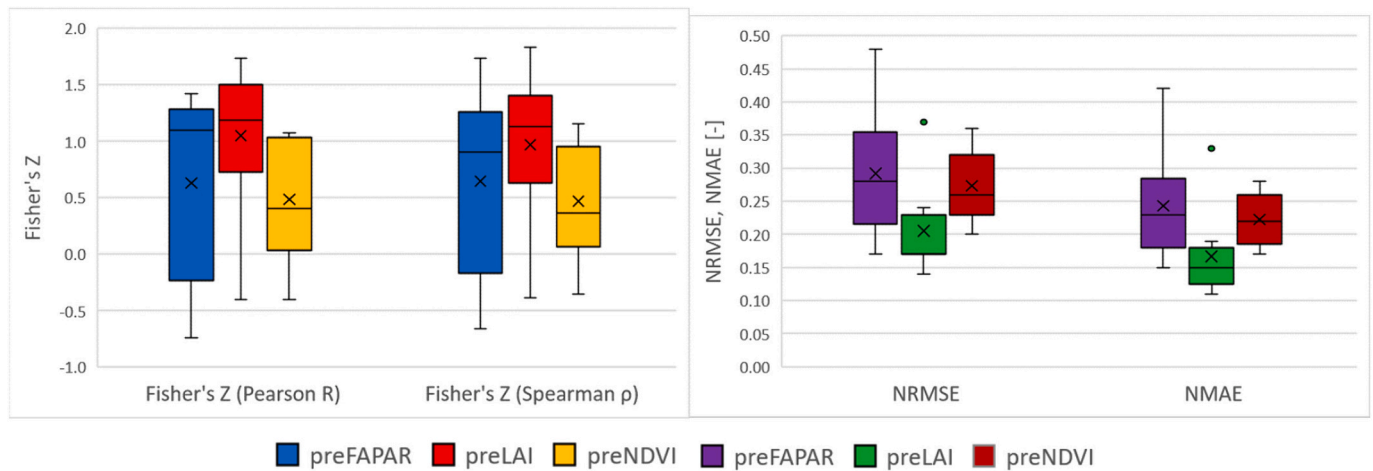

Fig. 7. Pearson, Spearman coefficients and normalised error metrics for correlating of LCC-MOGPR to OTCI data through 2020 and 2021. The assessment of results by both R, ρ yields a comprehensive analysis of the monotonic and linear correlation between datasets.

Fig. 8. Boxplots for the distributions of the Pearson (*R*) and Spearman (*ρ*) correlation coefficients Fisher's Z transformed form for LCC-MOGPR against OTCI data. Normalised error metrics (NRMSE, NMAE) are shown for reconstructed LCC-MOGPR to OTCI correlation. To allow for an adequate comparison between coefficients, these boxplots plot the Fisher Z transformed coefficients. × marks the mean, whereas the horizontal line in the boxes refers to the median.
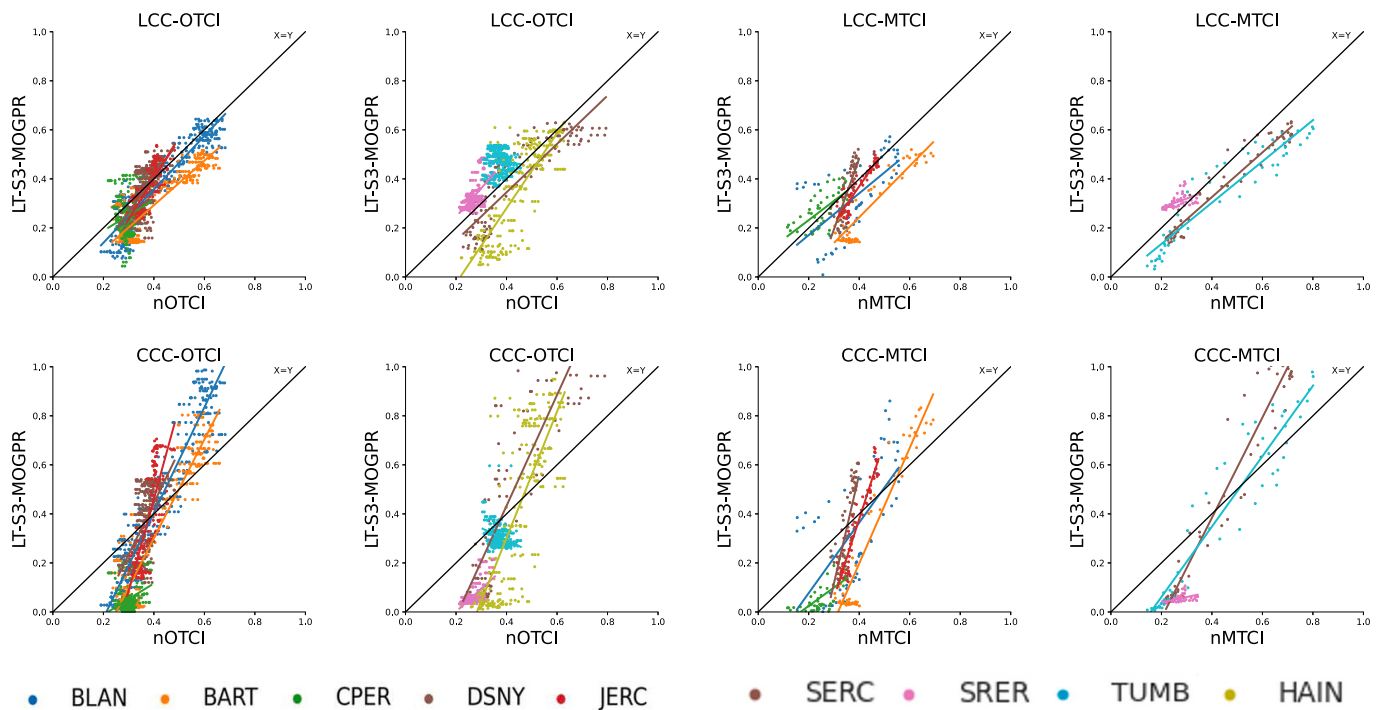
Fig. 9. Scatter plots of LCC-MOGPR with upscaled CCC reconstructed by preLAI compared to normalised OTCI data throughout 2020–21, and to normalised MTCI over 2010–11 over nine GBOV sites.

Table 4
Statistical metrics for comparing LCC to MTCI (2010−11) and OTCI (2020−21). Note, that TUMB does not feature available MTCI retrievals within the 2010−11 timeframe. R an Rho for the LCC-OTCI comparison are indicated in Fig. 7.

LCC	OTCI			MTCI					
	Bias	N	Precision	R	rho	Bias	N	Precision	NRMSE
BLAN	−0.04	370	0.07	0.63	0.7	−0.06	58	0.12	0.13
BART	−0.11	354	0.06	0.9	0.67	−0.15	63	0.06	0.17
CPER	−0.05	298	0.08	0.67	0.67	0.02	49	0.05	0.06
DSNY	−0.01	365	0.07	0.8	0.81	0	63	0.08	0.08
JERC	−0.01	182	0.06	0.92	0.9	−0.03	63	0.04	0.05
SERC	−0.06	129	0.09	0.97	0.94	−0.08	57	0.05	0.09
SRER	0.06	289	0.04	0.52	0.73	0.04	62	0.03	0.05
TUMB	0.09	366	0.07	–	–	–	–	–	–
HAIN	−0.09	237	0.12	0.95	0.96	−0.1	51	0.07	0.12

showcasing improvements over several sites for both OTCI and MTCI. However, CCC shows systematic over-underestimation as compared to normalised values of OTCI and MTCI. The greatest differences between the correlation to OTCI and MTCI for the CCC data streams were observed over the CPER site, where *R* values for the MTCI comparison doubled as compared to OTCI.

3.4. S3-MOGPR time series with uncertainties and reference products

As described in Section 3.2, the most consistent S3-MOGPR reconstruction results against the CGLS and OTCI/MTCI reference product were obtained by using preLAI from MODIS. These temporal profiles with the associated epistemic (i.e., model-based) uncertainty of the MOGPR method are also plotted as a blue-shaded region over the mean back prediction of each time series. The uncertainty is generally lower for sites with higher seasonal variation in the amplitude of the profiles. Note how LCs such as evergreen broadleaf (TUMB) and shrublands (SRER) that exhibit low yearly changes in vegetation dynamics depict higher associated uncertainties. For deciduous broadleaf and mixed forests (BLAN, BART, HAIN in Appendix A) and croplands (SERC) the S3-MOGPR profiles generally show reliable performance with the CGLS benchmarking as well as ground-based reference products, with a slight negative bias through the end-of-season. For open shrublands and evergreen needle leaf (JERC, DSNY in Appendix A), less seasonality is present, and the results also compare adequately to reference measurements, with increased fluctuations over DSNY, and systematic overestimations in the case of LAI-MOGPR for JERC. Closed shrublands and evergreen broadleaf forests (SRER, TUMB both in Appendix A) all show reduced seasonal vegetation dynamics and deviated in satellite and ground-based comparisons for these LCs. These sites are all characterized by LCs that do not exhibit a pronounced cyclical change throughout the year. The epistemic MOGPR uncertainty for such LCs is also larger as compared to ones with more seasonal variations (e.g. SERC, BLAN).

LCC-MOGPR profiles tend to capture vegetation seasonality better than OTCI, as seen on Fig. 10. When comparing the two time series, LCC-MOGPR shows a more realistic end-of-season minimum for deciduous broadleaf forests (BLAN) and croplands (SERC) reaching close to zero values, whereas OTCI stays relatively high. Seasonal peaks are well captured by both LCC-MOGPR and OTCI reaching similar yearly maximas. The CCC temporal profiles show similar seasonal characteristics to both OTCI and MTCI, which can be expected due to the nature of these indices being surrogates for canopy scale chlorophyll contents. Fig. 10 presents the S3-MOGPR reconstructed time series (FAPAR, FVC, LAI, and LCC) processed with MODIS-based preLAI, along with the reference datasets (both CGLS, OTCI and ground-based measurements) plotted.

3.5. Non-reconstructed S3 based VP validation

To provide a solid basis for the assessment of the reconstructed MOGPR products, the non-reconstructed S3 OLCI based vegetation products retrievals were validated. The data represented in Fig. 11 and Tables 6 show the comparison between the data streams retrieved S3 OLCI without the MOGPR temporal reconstruction applied. The correlation statistics were obtained not only in 2019, but for some sites in 2020 and 2021 where measurements were available. As it could be expected, the harmonized MODIS-S3 OLCI results present superior validation statistics for several sites, mainly benefiting from the supplementary information provided by the additional sensor (Trevisiol et al., 2024). One particular caveat is the TUMB site, where the MOGPR

reconstructed time series correlation to reference data heavily deteriorated for FVC and LAI. S3 based LAI data shows some slight overestimations (positive bias) as compared to GBOV measurements. Generally, FVC and LAI tend to show better agreement than FAPAR to in situ data.

3.6. Validating S3-MOGPR to ground measurements

To further evaluate the integrity of the generated S3-MOGPR temporal profiles and to bypass the satellite-based retrievals' inconsistencies for the reference products, our results were validated with in-situ ground reference measurements. As investigated in Section 3.2 the most robust reconstruction methodology was to use MODIS preLAI as predictor input; thus, the resulting profiles by using preLAI were validated against in-situ reference measurements at the nine locations, as described in Table 3. The correlation coefficients after validation show overall good agreement results. Fig. 12 depicts scatter plots between the FAPAR, FVC, and LAI-MOGPR, and ground-based measurements. Corresponding correlation coefficients and error statistics were calculated, as shown in Table 7. The highest correlations were achieved over JERC and SERC for FVC-MOGPR ($R = 0.93$). Furthermore, the results indicate generally good agreement. SERC exhibited the highest correlation for all reconstructed variables ($R, \rho \geq 0.84$). Additionally, BLAN, CPER, JERC, and HAIN indicated $R, \rho \sim 0.7$ for all reconstructed variables. The largest accuracy deviations were noted over SRER where *R* values were approximately three times larger for reconstructed FAPAR and FVC than LAI. The lowest agreements were obtained over TUMB for all variables, while the reconstructed FVC still showed moderate correlation metrics ($R = 0.56$). Reconstructed FAPAR was the only S3-MOGPR variable to depict negative correlations when comparing its linear and monotonic relationship to in-situ data over TUMB. This is also apparent when investigating the gradient of best-fit lines for correlation for these two sites in Fig. 12. Comparing the reconstructed time series by the MOGPR harmonization, one can note that several statistical metrics have improved. Pearson correlations have improved over BART, DSNY, JERC and SRER when using harmonized, reconstructed data for FAPAR, FVC and LAI too. Furthermore, UAR values show better agreements over JERC and SERC, especially for the reconstructed LAI data streams. Differences in biases were minor in magnitude after the MOGPR reconstruction.

3.7. Reconstructed maps

Following, the MOGPR algorithm was run sequentially to produce S3-like VPs maps, reconstructing time series for multiple pixels at 500 m spatial resolution for the year 2015, before S3's launch to showcase the MOGPR algorithm's past data reconstruction capability. The resulting maps (44, at 8 days resolution) were composited monthly, and four months are shown with distinct growing stages for vegetation. Fig. 13 and 14 were selected for mapping as these sites involve different types of vegetation cover in their vicinity. Fig. 13 shows grassland and cropland-dominated areas near CPER, whereas Fig. 14 entails mixed forests and croplands in the 50 km radius region of the HAIN site. Reconstructing vegetation patterns a year before S3's launch demonstrates the MOGPR algorithm's ability to accurately capture seasonal variations in vegetation across different land cover types. The peak of the growing season over the croplands, located just south of the CPER station (Fig. 13), is prominently visible on all variable's June maps. Evergreen forests, south-east from the HAIN site, present relatively low seasonal fluctuations of their foliage, this is also well represented in Fig. 14.
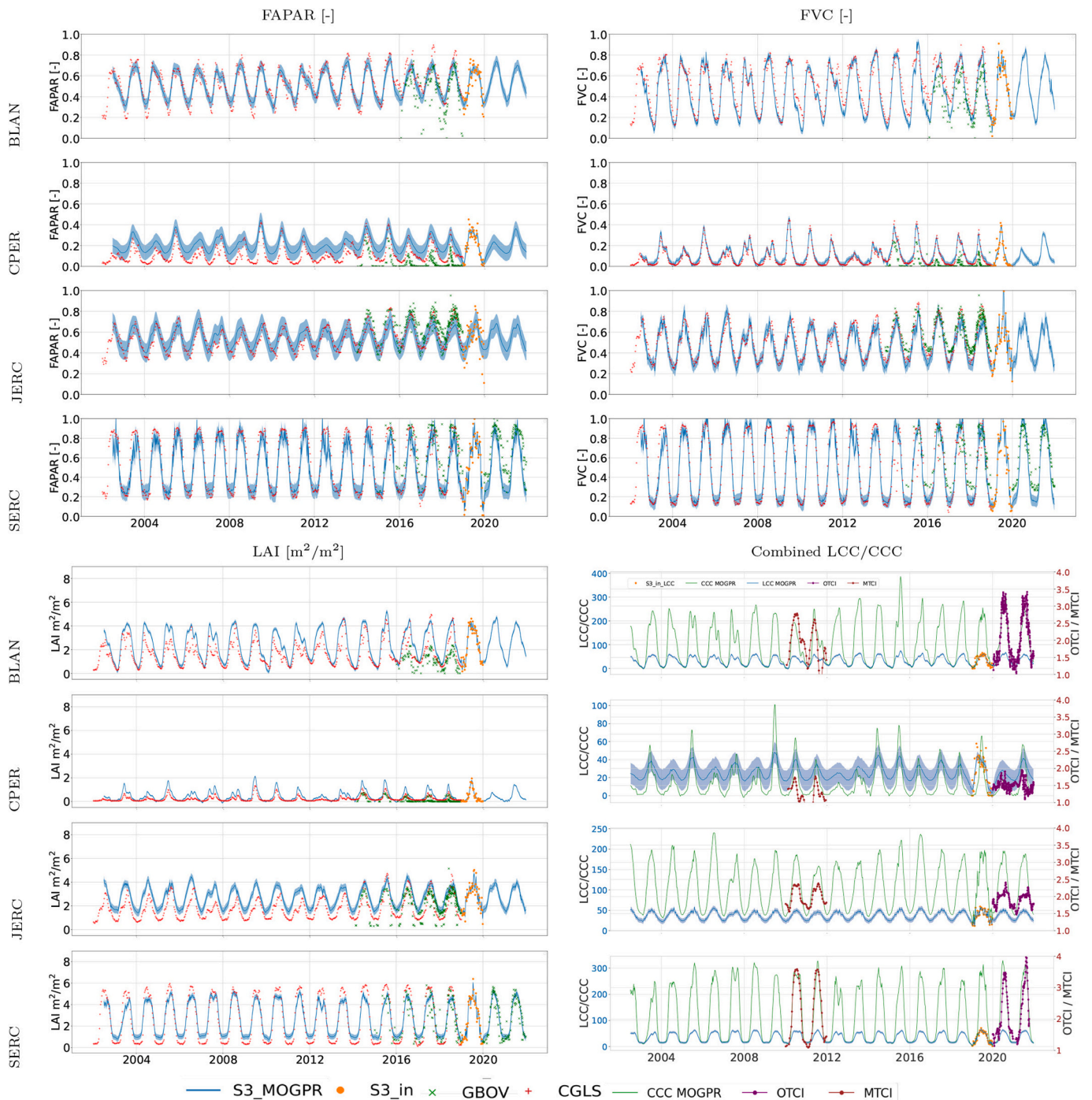
Fig. 10. Temporal profiles over BLAN, CPER, JERC, and SERC depicting S3-MOGPR variables for the 2002–2022 window with uncertainties. CGLS, M/OTCI, and GBOV in-situ reference measurements are plotted. Yellow dots indicated the training S3 data to the MOGPR algorithm in 2019. PreLAI is used as a predictor variable. The temporal profiles for BART, DSNY, SRER, TUMB, and HAIN are shown in Appendix A. (For interpretation of the references to colour in this figure legend, the reader is referred to the web version of this article.)
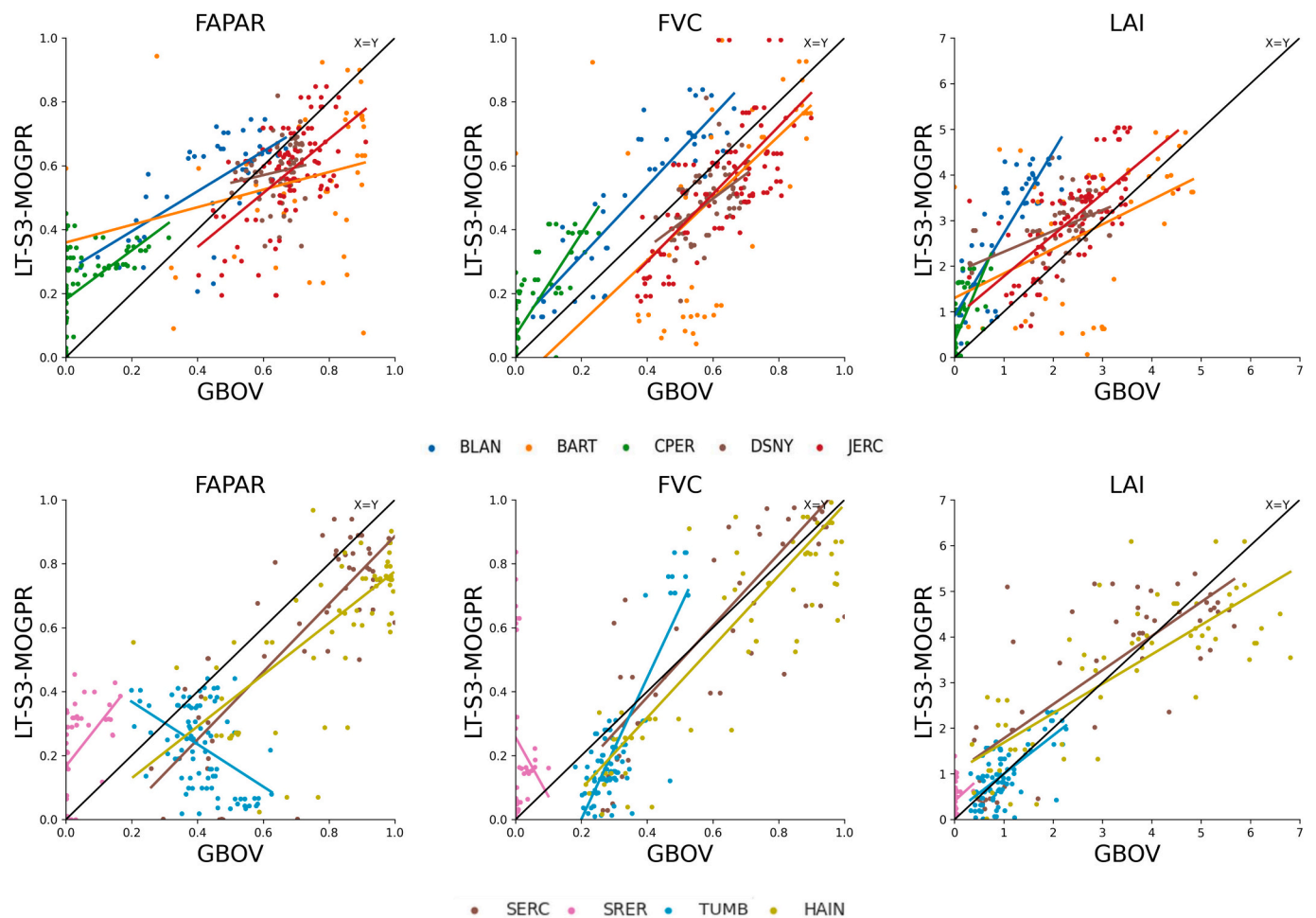
Fig. 11. Scatter plots depicting the relationship between the S3 OLCI based FAPAR, FVC, and LAI retrieved on real scenes and in-situ reference measurements.

Table 6
Validation statistical metrics recommended by good practice (Fernandes et al., 2014) when validating S3 OLCI based FAPAR, FVC and LAI on real S3 scenes.

S3 real scenes	FAPAR			FVC			LAI		
	R	Rho	NRMSE	R	Rho	NRMSE	R	Rho	NRMSE
BLAN	0.67	0.59	0.16	0.89	0.84	0.17	0.83	0.83	1.95
BART	0.27	0.36	0.31	0.56	0.65	0.31	0.45	0.43	1.55
CPER	0.46	0.53	0.21	0.78	0.77	0.13	0.65	0.72	0.71
DSNY	0.16	0.23	0.12	0.51	0.55	0.14	0.48	0.57	0.99
JERC	0.57	0.47	0.15	0.73	0.72	0.16	0.71	0.73	0.96
SERC	0.80	0.66	0.22	0.83	0.77	0.19	0.79	0.71	1.19
SRER	0.48	0.48	0.22	−0.15	0.29	0.35	0.16	0.48	0.53
TUMB	−0.47	−0.43	0.27	0.86	0.58	0.17	0.66	0.55	0.48
HAIN	0.67	0.70	0.26	0.82	0.75	0.21	0.79	0.76	1.20

| S3 real scenes	FAPAR				FVC			LAI			
	Bias	N	Precision	UAR	Bias	N	Precision	Bias	N	Precision	UAR
BLAN	0.1	46	0.13	0.24	0.13	46	0.11	1.73	45	0.9	0.16
BART	−0.16	44	0.26	0.18	−0.1	47	0.29	−0.05	42	1.54	0.24
CPER	0.17	102	0.12	0.18	0.09	102	0.09	0.48	96	0.52	0.59
DSNY	−0.06	63	0.1	0.38	−0.1	63	0.09	0.72	61	0.69	0.36
JERC	−0.1	105	0.12	0.28	−0.09	105	0.14	0.64	103	0.71	0.39
SERC	−0.13	52	0.17	0.19	0.01	52	0.19	0.29	51	1.15	0.33
SRER	0.18	49	0.12	0.22	0.22	49	0.27	0.41	49	0.33	0.61
TUMB	−0.19	90	0.19	0.17	−0.07	90	0.15	0	87	0.48	0.72
HAIN	−0.18	75	0.19	0.11	−0.05	75	0.21	−0.16	74	1.19	0.31
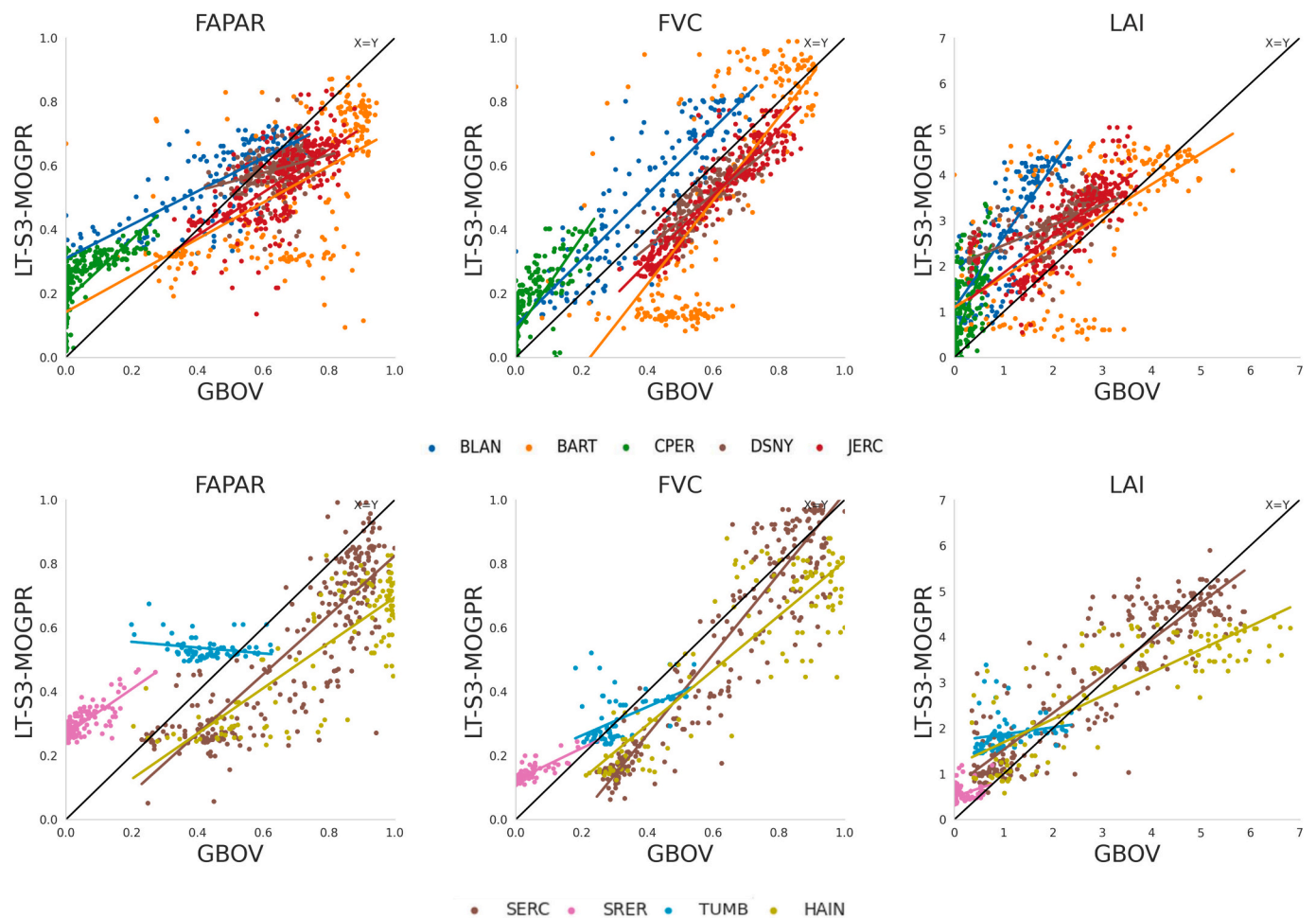
Fig. 12. Scatter plots depicting the relationship between the MOGPR reconstructed FAPAR, FVC, and LAI and in-situ reference measurements. For the site-specific temporal windows used for validation consult Table 3.

Table 7
Correlation coefficients and error metrics recommended by good practice (Fernandes et al., 2014) calculated by validating S3-MOGPR reconstructed to in-situ measurements. For the site specific temporal windows used for validation consult Table 3.

	FAPAR				FVC				LAI			
	R	rho	NRMSE	NMAE	R	rho	NRMSE	NMAE	R	rho	NRMSE	NMAE
BLAN	0.75	0.77	0.14	0.12	0.88	0.88	0.14	0.12	0.82	0.84	0.19	0.17
BART	0.6	0.61	0.24	0.2	0.74	0.72	0.26	0.22	0.61	0.56	0.14	0.10
CPER	0.68	0.77	0.2	0.18	0.78	0.81	0.1	0.09	0.69	0.73	0.09	0.06
DSNY	0.34	0.42	0.1	0.07	0.83	0.84	0.1	0.09	0.64	0.75	0.11	0.09
JERC	0.68	0.73	0.14	0.11	0.93	0.92	0.1	0.1	0.79	0.84	0.09	0.07
SERC	0.86	0.84	0.2	0.16	0.93	0.9	0.14	0.13	0.9	0.86	0.08	0.06
SRER	0.81	0.73	0.26	0.25	0.84	0.82	0.1	0.11	0.36	0.53	0.05	0.05
TUMB	−0.25	−0.19	0.14	0.12	0.56	0.51	0.1	0.05	0.2	0.51	0.10	0.09
HAIN	0.83	0.71	0.26	0.25	0.88	0.76	0.2	0.16	0.82	0.76	0.13	0.10

	FAPAR				FVC				LAI			
	Bias	N	Precision	UAR	Bias	N	Precision	UAR	Bias	N	Precision	UAR
BLAN	0.09	115	0.12	0.27	0.1	115	0.1		1.66	112	0.79	0.11
BART	−0.14	171	0.17	0.18	−0.11	171	0.22		0.32	134	1.27	0.39
CPER	0.18	276	0.05	0.02	0.09	277	0.06		0.44	227	0.32	0.64
DSNY	−0.04	168	0.07	0.49	−0.08	168	0.06		0.97	162	0.56	0.2
JERC	−0.1	221	0.07	0.21	−0.09	221	0.06		0.65	199	0.53	0.48
SERC	−0.16	224	0.13	0.18	−0.08	224	0.12		0.15	212	0.75	0.56
SRER	0.25	165	0.03	0	0.11	165	0.02		0.47	154	0.17	0.62
TUMB	0.1	80	0.09	0.22	0	80	0.08		0.82	80	0.58	0.25
HAIN	−0.25	142	0.12	0.02	−0.15	142	0.11		−0.5	134	1.2	0.32
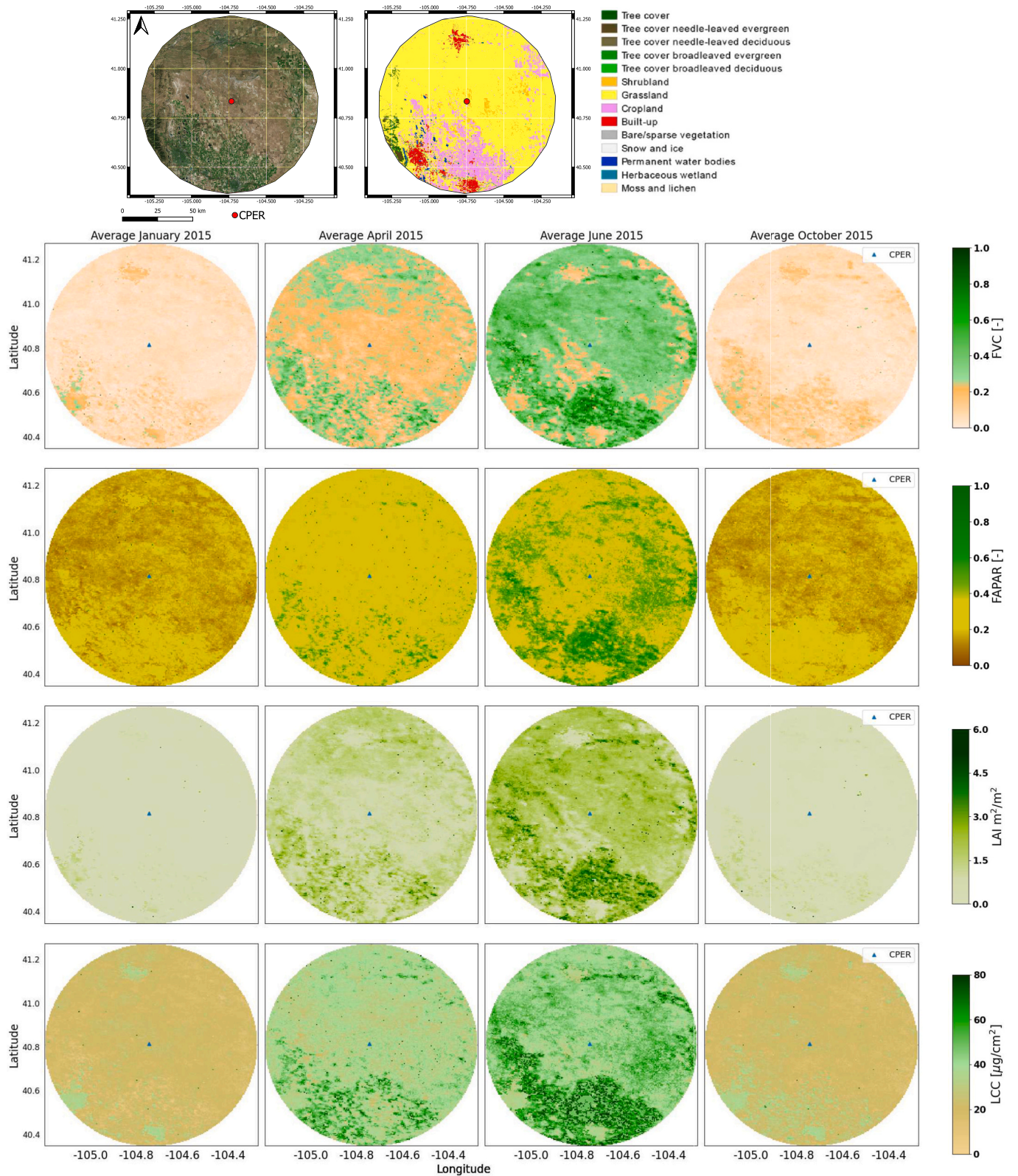
Fig. 13. Temporally reconstructed maps for the four VPs throughout the year 2015. The maps are centered at the CPER site (lat: 40.815, long: −104.745) and a 50 km radius area is plotted. RGB imagery and land cover maps are shown for the investigated area.
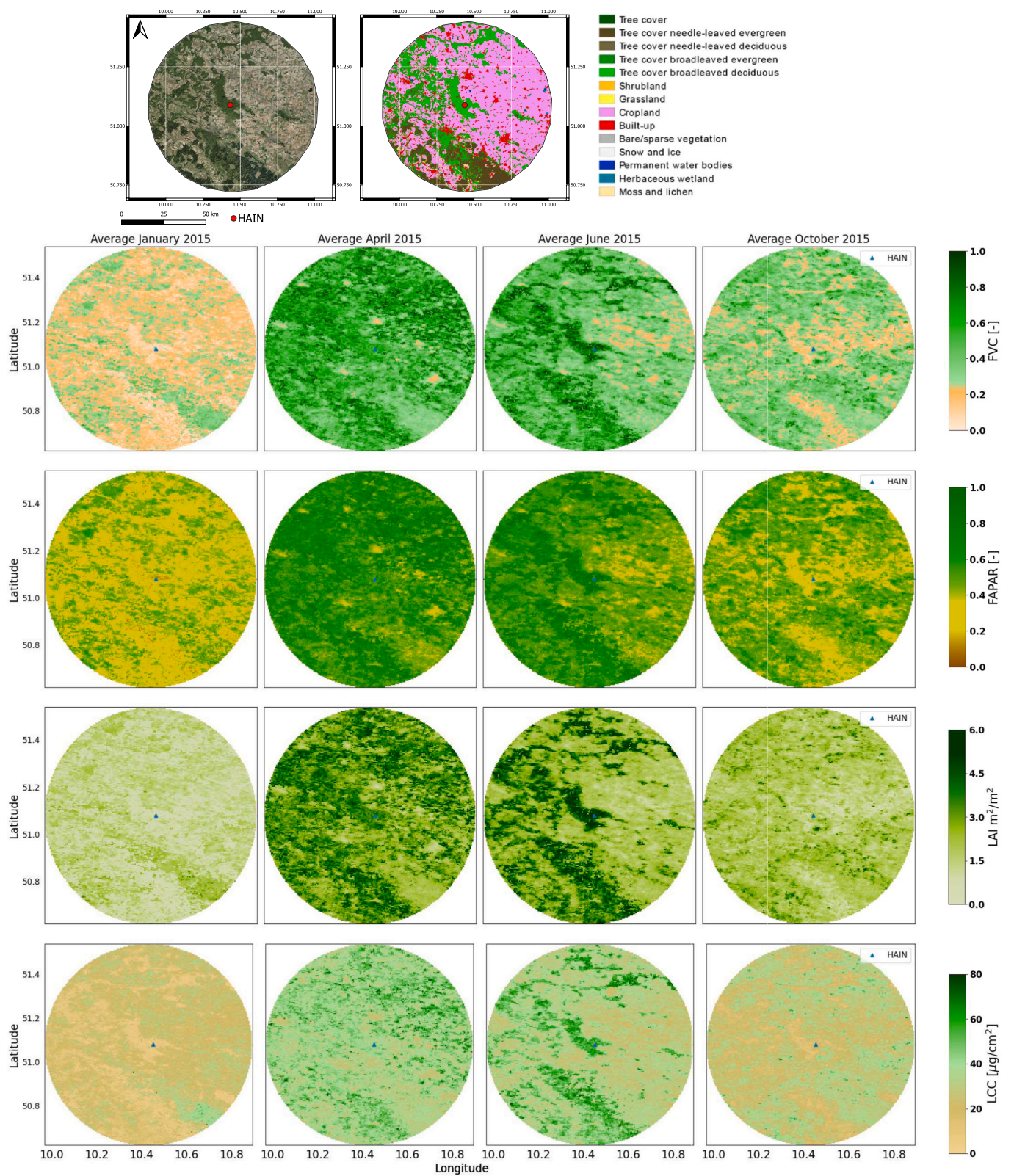
Fig. 14. Temporally reconstructed maps for the four VPs throughout the year 2015. The maps are centered at the HAIN site (lat: 51.079, long: 10.452) and a 50 km radius area is plotted. RGB imagery and land cover maps are shown for the investigated area.

Additionally, to assess the consistency of the reconstructed maps a year prior to S3's launch, the spatio-temporal datasets presented on Fig. 14 and 13, were per pixel intra-annually correlated to CGLS products (Fuster et al., 2020), as seen on Fig. 15. No major differences can be noted when comparing the correlation maps between different variables. For CPER the agreement is higher as compared to CPER for all variables. Over HAIN, some negative correlation can be observed on the south-eastern side of the circular ROI. This area is covered by evergreen needleleaf forests, usually depicting lower intra-annual seasonality.

4. Discussion

Aiming to generate S3-consistent, multi-decadal ECVs, we propose a flexible methodology to reconstruct long-term past time series by using MOGPR fusion guided by complementary MODIS products. The systematic analysis evaluates the outcome of past biophysical variable data
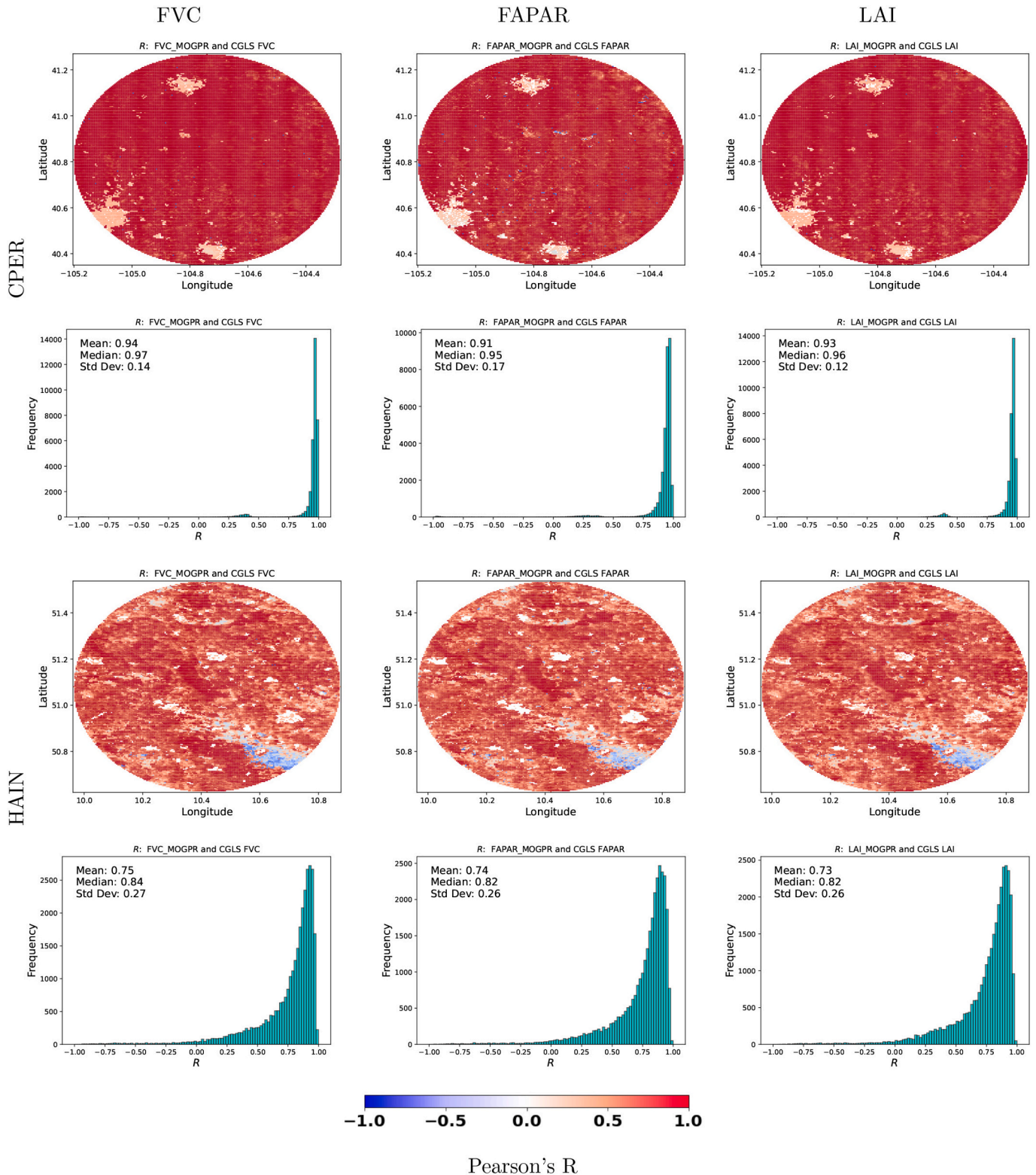

Fig. 15. Per pixel intra-annual Pearson correlation maps over the CPER and HAIN site in 2015.

reconstruction (S3-based FAPAR, FVC, LAI, and LCC) by different MODIS-based predictor time series (MODIS-based preFAPAR, preLAI, and preNDVI). Our MOGPR-based reconstruction approach, despite relying on predictor data from MODIS products that exhibit inherent differences compared to S3 due to advancements in technology, hardware, and retrieval algorithms and crucially for LCC the missing red-edge bands, successfully provides harmonized, temporally consistent data streams of LAI, FAPAR, FVC, and LCC time series. In the following, we discuss the performance of the MOGPR-reconstructed products compared to satellite benchmark products and ground data and provide limitations, challenges, and opportunities for our models.

4.1. Performance of different predictor variables in MOGPR fusion

The S3-based reconstructed time series products realized by distinct predictor variables (Fig. 4) showed varying results. Both preNDVI and preFAPAR from MODIS propagated more noise to nearly all S3-MOGPR sites and variables. The resulting S3-MOGPR variables' data streams could produce erroneous output owing to the propagation of the preVars noise, amplitude, and cyclic properties throughout when using ML methods to model time series (Dera et al., 2023). The profiles reconstructed by preNDVI are more susceptible to noise as compared to those predicted by preLAI. Constrained by the use of only two bands, NDVI is potentially vulnerable to noise from sensor calibration, atmospheric attenuation, clouds, and off-nadir viewing angles, resulting in (non-seasonal) fluctuations in its temporal profiles (Goward et al., 1991; Hird and McDermid, 2009). Another limitation of NDVI is its saturation at canopies having LAI values of ∼3–4 (Yan et al., 2022), becoming insensitive at denser vegetation (Ferrara et al., 2010; Gitelson, 2004). Alternatively, instead of NDVI, the MODIS vegetation continuous fields (VCF) and other spectral indices could have been selected as the guiding predictor variable, such as the enhanced vegetation index (EVI), which may be less prone to saturation in dense vegetation (Carroll et al., 2011; Huete et al., 2002). The bottom line is to identify a predictor variable that follows as closely as possible to the temporal profile of the targeted variable. Here, the presented workflow showcased the MOGPR algorithm's ability to extrapolate and reconstruct temporal profiles with MODIS-based LAI, FAPAR and NDVI, as these are three independent vegetation products. Follow-up research could evaluate the role of alternative ancillary predictors (such as EVI) data for guiding time series harmonization.

FAPAR time series retrieved by MODIS have considerable noise, as also noted by (Camacho et al., 2013). FAPAR, in its nature, entails the absorbed incoming radiation; it elicits the question of the diurnal variation of its value by the varying Solar Zenith angle (SZA) (Tran et al., 2020; Widlowski, 2010). Because FAPAR varies with weather conditions and incoming radiation and most FAPAR products correspond to values at the satellite transmit time only (instantaneous FAPAR), the observed FAPAR values are subject to the uncertainties induced by the aforementioned factors (Chen et al., 2020; Moreno et al., 2014). Such fluctuations in the temporal domain can propagate higher uncertainties into the reconstruction algorithm, and the time series prediction becomes fundamentally difficult for high noise profiles, as also observed by Giles et al. (2001); Johnson et al. (2019). The MOGPR algorithm ultimately reconstructed past data records with increased consistency when less noise and fluctuations were presented in the training dataset's predictor variable, as also investigated by Villacampa-Calvo et al. (2021). The profiles with the fewest fluctuations for S3-MOGPR were retrieved by using preLAI. However, some studies demonstrated that also MODIS LAI temporal profiles can be prone to noise (Brown et al., 2020; Fuster et al., 2020; Yan et al., 2024).

Especially interesting is the temporal reconstruction of LCC from preLAI, as LCC and LAI typically present a different seasonal behaviour with maximums of LCC occurring later than LAI, as shown in Brown et al. (2019b); Wang et al. (2021). Notably, the reconstructed S3-MOGPR data over TUMB exhibits inconsistent patterns across all predictor variables. This can be explained by the lack of a marked seasonality (nor a stationary state), which compromises the predictive capacity of S3-MOGPR over time.

4.2. Consistency of S3-MOGPR products against CGLS reference data

The S3-MOGPR-generated products indicated consistency over diverse locations and LCs when compared to the reference CGLS dataset (FAPAR, FVC and LAI). The high R, ρ correlations can generally be linked to strong seasonality. This is visible when investigating Table 5, where the highest correlations between S3-MOGPR products and the satellite-based reference dataset were obtained over sites with LCs such as deciduous, mixed forests and croplands (BLAN, BART, SERC and HAIN depicting $R, \rho \sim 0.9$ for FAPAR, FVC and LAI).

The overall strong correlation between FAPAR and LAI yields optimal performance when using these variables mutually (reconstructed-predictor) (Roujean and Lacaze, 2002). FAPAR being a physiological variable, and LAI adding information on the physical structure, are both correlated with the green vegetation captured by satellites. This can be noted when addressing the higher correlation of the reconstructed FAPAR and LAI when they are predicted by preFAPAR or preLAI, rather than by preNDVI (see Fig. 6).

When correlating the reconstructed S3-MOGPR variables obtained by preNDVI to CGLS, NDVI as a predictor variable yields better results over sparse canopies as opposed to the higher density of the vegetation (forest) stands, which often leads to saturation of the spectral recordings (Mutanga et al., 2023), as exhibited in Table 5 over TUMB, showing the lowest correlations for preNDVI-based reconstruction for all S3-MOGPR variables. An NDVI value may be the result of unknown variability of vegetated ground cover (e.g., different values for FVC and LAI) and clumped leaf area (Myneni and Williams, 1994), thus propagating uncertainties to the relationship between NDVI, LAI, and FVC. This is apparent in the generally lower correlations when reconstructing S3-MOGPR variables by preNDVI.

Typically, similar values were obtained for linear (R) and monotonic (ρ) relationships between S3-MOGPR and CGLS data streams, except for the site BART, where R values were generally greater by 0.1 than ρ. This could be because the time series of CGLS captures the growing season earlier than the MODIS-based S3-MOGPR reconstruction, as the CGLS product shows an earlier start of the growing season (see BART in Appendix A). This causes a deviation between the S3-MOGPR and CGLS time series, especially over the growing season, ultimately indicating a lower monotonic correlation and higher non-linearity between the two temporal profiles.

The reconstructed maps provide a visual representation of the applicability of the MOGPR algorithm to sensor harmonized maps. The correlation to CGLS data streams, duly validated by (Fuster et al., 2020), show promising results, achieving higher overall correlation over CPER where all variables yielded mean R of greater than 0.9. Interestingly, the maps over CPER yielded better correlation metrics than for HAIN, due to the land cover heterogeneity within the vicinity of the HAIN site. Land cover heterogeneity exacerbates VP retrieval performance, as also noted by (Gelybó et al., 2013).

4.3. Assessing the validation S3-MOGPR products to ground data

To assess the validity of the generated S3-MOGPR products, matching values were compared against ground measurements (Fig. 12) and their error metrics were calculated, as shown in Table 3. The best validation statistics were achieved over SERC for all variables, with FVC showing the highest correlation of $R, \rho = 0.93, 0.9$. For croplands (SERC), slight systematic underestimation, (with biases of −0.16, −0.08 respectively) can be observed for FAPAR-, FVC-MOGPR products during winter, similarly to the findings of Chernetskiy et al. (2017). This negative bias increased by the reconstruction procedure algorithm. In this case, the MOGPR models do not detect the predominant presence of

bare soil or that it is contaminated by a heterogeneous signal. The presented validation error metrics for FVC-MOGPR are in the same order as the ones reported by Ding et al. (2015). As complementary to LAI, FVC measures the horizontal extension of vegetation, where saturation or clumping effects do not occur. FVC outperforming LAI and FAPAR through in-situ validation was also noted by Upreti et al. (2019).

Over sites with croplands (SERC), deciduous (BLAN), and mixed forests (HAIN in Appendix A) all reconstructed variables showed consistency $R, \rho > 0.75$. The good validation statistics over these LCs were also noted by Yan et al. (2016). Over BLAN, systematic positive bias was noted for all three variables, in agreement with Camacho et al. (2013) who reported similar biases for LAI. For SERC and HAIN a slight negative bias could be observed. Lower correlations were obtained over the evergreen broadleaf forests of TUMB. The lack of accurate retrievals as compared to ground measurements over such land covers was also noted by Kang et al. (2021) when evaluating various VPs against in-situ data. This land cover type exhibits lower seasonal phenological dynamics, which is hardly captured by the satellite-based VPs (Verger et al., 2023). Cloud contamination, poor atmospheric conditions, and radiative signal saturation further exacerbate this issue (Yan et al., 2016).

4.4. Chlorophyll variables' comparison against the OTCI and MTCI datasets

The scarcity of global LCC datasets and in-situ reference measurements impeded direct validation of the LCC-MOGPR product. Having explored different LCC products (e.g. from Croft et al. (2020b) and Xu et al. (2022)), in our experience these products were perceived as unreliable for comparison, showcasing highly irregular time series. The MODIS-based LCC product provided by Xu et al. (2022) was evaluated as unreliable. The authors discussed the limitation of inferring LCC from MODIS due to the missing red-edge band, and this was further supported by Kovács et al. (2023b) where the tested MODIS-based LCC dataset proved to be poorly performing. We also inspected the LCC product by Croft et al. (2020b) and observed irregular temporal patterns, which made the product untrustworthy for comparison analysis. Notwithstanding, we utilized the OTCI and MTCI land products as a sound benchmark due to their strong relation to vegetation (canopy) chlorophyll content (Pastor-Guzman et al., 2020). Estimating leaf-level variables, such as LCC, is generally more challenging than retrieving canopy-level variables, such as LAI or FAPAR, from EO data, caused by the complex relationship between leaf characteristics and canopy-scale reflectance (see e.g., discussion in Estévez et al. (2021)). Therefore, the error metrics in Table 7 and 8 portray higher overall normalised errors as compared to the case of FAPAR, FVC, and LAI-MOGPR to CGLS products. Despite these, the preLAI-based LCC-MOGPR showed high consistency when correlating to normalised OTCI/MTCI over most sites except for TUMB. The upscaled CCC product, at the canopy scale, shows mildly improved agreements to reference data, as it could be expected. Even though LCC-MOGPR, OTCI and MTCI are indicators of chlorophyll content, their calculations are based on completely different algorithms. While OTCI/MTCI is a rather simple 3-band spectral index (empirical approach), LCC is based on physical equations in an RTM embedded within a hybrid retrieval scheme (see Reyes-Muñoz et al. (2022)). Overall, the reconstructed LCC and CCC product showed high consistency with OTCI/MTCI datasets for both linear (R) and monotonic (ρ) relationships across sites exhibiting distinct seasonal variations. Notably, the highest correlation metrics were observed among deciduous broadleaf (BLAN) and mixed forests (HAIN in Appendix A), aligning with the findings of Croft et al. (2020a). Generally, the LCC-MOGPR

profiles display a more realistic trend over the winter, whereas OTCI tends to overestimate and not reach such yearly minimums (Pastor-Guzman et al., 2020). Some discrepancies could be observed for CCC when compared to the reference indices, possibly resulting from the nature of the two products and their normalisation strategies.

4.5. MOGPR associated uncertainties

The usage of MOGPR for time series reconstruction enables the quantification of errors since it can generate predictions by integrating prior knowledge and offer measures of confidence intervals (uncertainties) for the predictions Wang (2023). Our presented algorithm showed minimal uncertainty over most sites for the reconstructed LAI, FVC, with few exceptions for LCC data records. The MOGPR algorithm could capture rapid phenological changes, often associated with uncertain outputs (McHutchon and Rasmussen, 2011) with minor deviations (see sites, e.g., BLAN, JERC, SERC, HAIN). This is due to that training the algorithm over a whole year allows for detecting the typical phenological changes with high precision. The MOGPR-associated uncertainties were nevertheless generally more notable for FAPAR-MOGPR reconstructed profiles. The increased uncertainty limit the retrieval accuracy and optimal temporal resolution of the S3-based FAPAR retrievals, thus inherently affecting the reconstruction uncertainty (Kovács et al., 2023b). MOGPR reconstruction-associated uncertainties can be also a result of ecological factors such as different LCs and land surface heterogeneity (Yu et al., 2018). When comparing the winter months over BART (in Appendix A) and BLAN (Fig. 10), it can be noted that the uncertainty of BART through winter is much larger than for BLAN for all reconstructed S3 variables. BLAN consists predominantly of deciduous broadleaf trees, whereas BART is a mixed forest of deciduous-to-boreal forest transitional ecotone (National Ecological Observatory Network (NEON), 2023), BART through winter exhibits more vegetation heterogeneity, ultimately resulting in increased uncertainty (Goldblum and Rigg, 2010; Wu et al., 2019). The effect of land surface heterogeneity-induced reconstruction uncertainty can also be noted over SRER, showing high uncertainties for reconstructed LCC, FVC, and FAPAR. SRER is a site dominated by drought-resistant, thorny vegetation, such as shrubs and perennial grasses, ultimately exposing greater soil surfaces (Network), N.N.E.O, 2023).

4.6. Limitations, challenges and opportunities

Consistent backward time series reconstruction before a mission's launch is a challenging task, but it is essential for a wide range of applications, such as tracking multi-decadal vegetation cover change patterns, which in turn can be related to climate change and biodiversity monitoring, and even economic analysis (Burgdorf et al., 2023; Privalsky and Gluhovsky, 2015). Despite its effectiveness in reconstructing multi-decadal, highly consistent time series, MOGPR's computational demands pose a significant challenge. For instance, reconstructing a single site-specific time series using 2vCPU @ 2.2GHz and 13GB RAM took approximately 2–3 min. The MOGPR fusion methodology requires a large matrix inversion (Das et al., 2018), thus the computational process is memory-heavy, leading to extended computational times (Caballero et al., 2023). By leveraging the openEO API to connect to a more powerful back-end provided by Terrascope (Terrascope, 2024, Accessed: 2024-03-27), the MOGPR algorithm achieved notable speed improvements. This enabled the processing of 50 km-radius circular maps within hours. Maps were produced at 8 days temporal resolution, thus 44 yearly maps were processed.

The presented MOGPR workflow opens several opportunities for further research and mapping applications, such as enlarging the spatial scale. To overcome the computational burden when progressing toward multi-decadal global maps, the presented workflow could be employed on high-performance computing, incorporating parallel computing environments (Gomes et al., 2020) and programming techniques (Sedona et al., 2019). Given the proven capability of the MOGPR algorithm to model the underlying interconnection between biophysical properties, its applications extend beyond past vegetation data record simulation. MOGPR-based multi-sensor fusion applications can be extended to various time series data streams to obtain consistent weather-related parameters (Wu et al., 2022), aid numerical weather prediction (Ren et al., 2021), improve tropical forest monitoring (Reiche et al., 2015) and model sea and land surface temperatures (Long et al., 2020; Ma and Kang, 2020). Moreover, the reconstructed multi-decadal ECV data streams can be a useful input into ecosystem sensitivity analysis, by assessing the response of ECVs' time series to environmental stressors (Kovács et al., 2023a; Papagiannopoulou et al., 2017) and studies on climate change (Brown et al., 2012; Trenberth et al., 2014).

The results indicate LAI to be a strong predictor for guiding the temporal reconstruction of different vegetation products. The time series reconstruction integrity could be improved with the involvement of ECVs given the underlying interconnection. For example, LAI has a proven effect on local micro-climate, thus opening up further opportunities to aid in the modelling of soil moisture, air temperature, and vapour pressure deficit (Von Arx et al., 2013). Moreover, using a more ample training dataset, with globally sampled LC-specific data for the site-specific local models, would lead to a better representation of extreme events, such as the fires over TUMB in early 2020 (Parker et al., 2021). Such events could cause drastic VP values, that would normally not occur in the training data over a regular year.

Finally, to further improve the consistency of the reconstructed products, the intra-sensor differences between MODIS and OLCI could be addressed, e.g., by employing cross-calibration of reflectances, atmospheric aerosol and Rayleigh scattering corrections before the retrieval of VPs, and so achieving cross-calibrated time series retrieved by the two sensors (Bojanowski et al., 2022). Also, for exploring advancements that further augment accuracy and processing speed, future work could address the comparison of the MOGPR method for data fusion and reconstruction against advanced neural network-based techniques, such as transfer learning that leverages the production of long-term LAI maps at fine resolutions (Zhou et al., 2023).

5. Conclusions

This study presents a flexible methodology for backward reconstructing key VP data streams from S3 data way before S3's launch in 2016 through time series fusion with guiding MODIS-based predictor variables. We evaluated three MODIS-derived predictor variables (FAPAR, LAI, and NDVI) on their ability to reconstruct data streams of S3-based biophysical and biochemical products (FAPAR, FVC, LAI, and LCC) for the past two decades (2002−2022). Using a fusion MOGPR algorithm with a long-term MODIS LAI data stream as the most effective guiding predictor variable, we successfully reconstructed a multi-decadal time series of S3-based LAI, FAPAR, FVC, and LCC. Validation against in-situ reference measurements at nine distinct land cover sites demonstrated the accuracy and consistency of the reconstructed VPs, with FVC particularly well captured. Despite the inherent differences between the nature of LCC and OTCI and MTCI, when reconstructed by MODIS-based LAI, the LCC-MOGPR profiles displayed more consistency when compared to OTCI, especially over croplands, deciduous broadleaf, and mixed forests. The consistency of the reconstructed data stream was mainly governed by vegetation seasonality, as the sites where lower intra-annual vegetation dynamics are present (e.g., evergreen broadleaf over TUMB) was poorly reconstructed. We conclude that the presented temporal reconstruction method can capture underlying interconnections between temporal data streams of biophysical variables and use this to reconstruct past data records given a guiding long-term data stream, such as MODIS. The presented MOGPR workflow addresses the limitations of S3's limited temporal record and paves the way for uninterrupted tracking of ECV dynamics over the past few decades. The workflow further opens up opportunities for consistent, long-term vegetation traits quantification, supporting multi-decadal monitoring of land-climate dynamics.

CRediT authorship contribution statement

Dávid D.Kovács: Writing – review & editing, Writing – original draft, Software, Formal analysis, Data curation, Conceptualization. **Pablo Reyes-Muñoz:** Software, Conceptualization. **Katja Berger:** Writing – review & editing, Writing – original draft, Formal analysis. **Viktor Ixion Mészáros:** Software. **Gabriel Caballero:** Writing – review & editing, Writing – original draft. **Jochem Verrelst:** Writing – review & editing, Writing – original draft, Formal analysis, Conceptualization.

Declaration of competing interest

None.

Data availability

The code used for the processing of the S3-MOGPR temporal profiles can be viewed and run by accessing the following repository: https://github.com/daviddkovacs/MOGPR-time-series-reconstruction/tree/main.

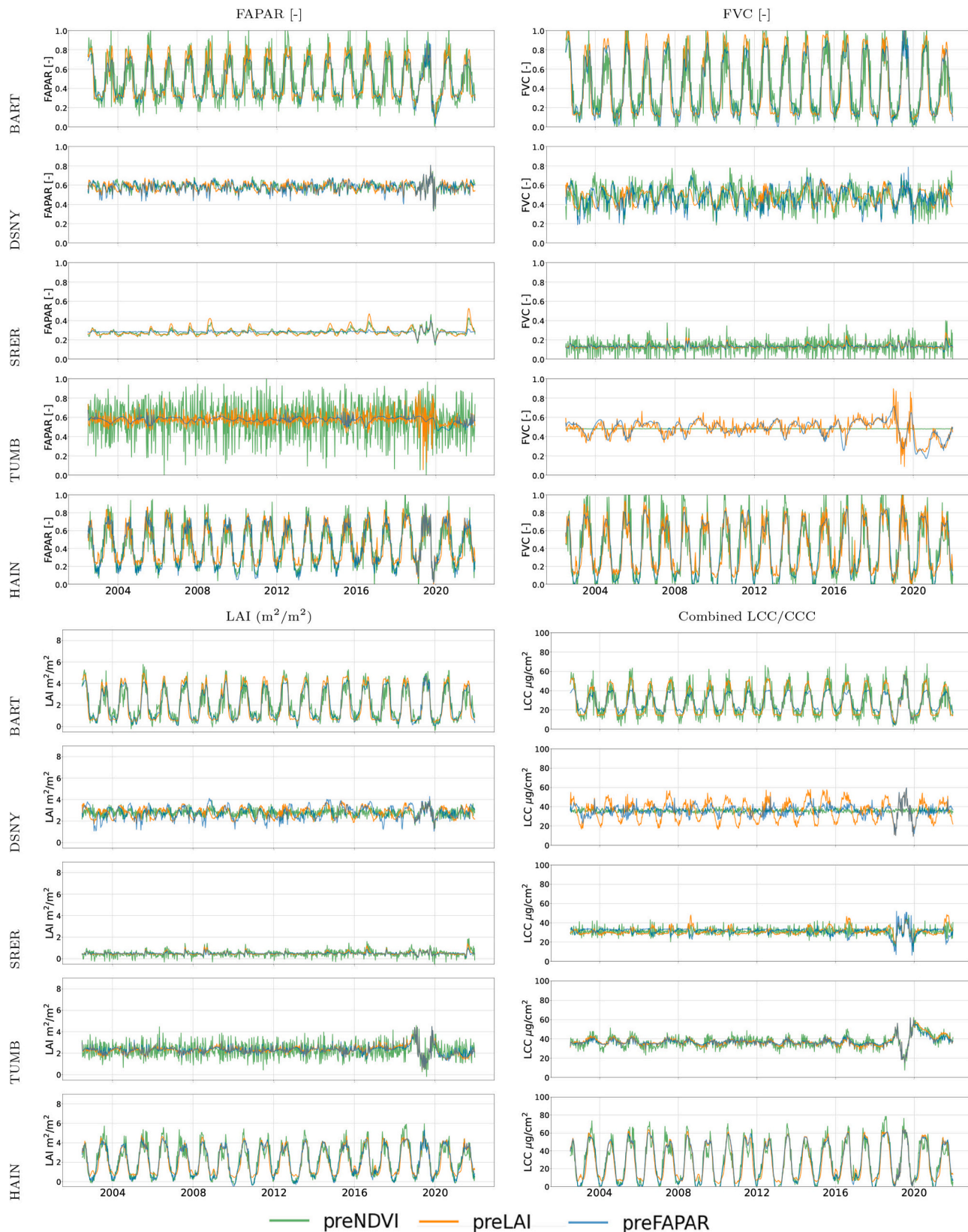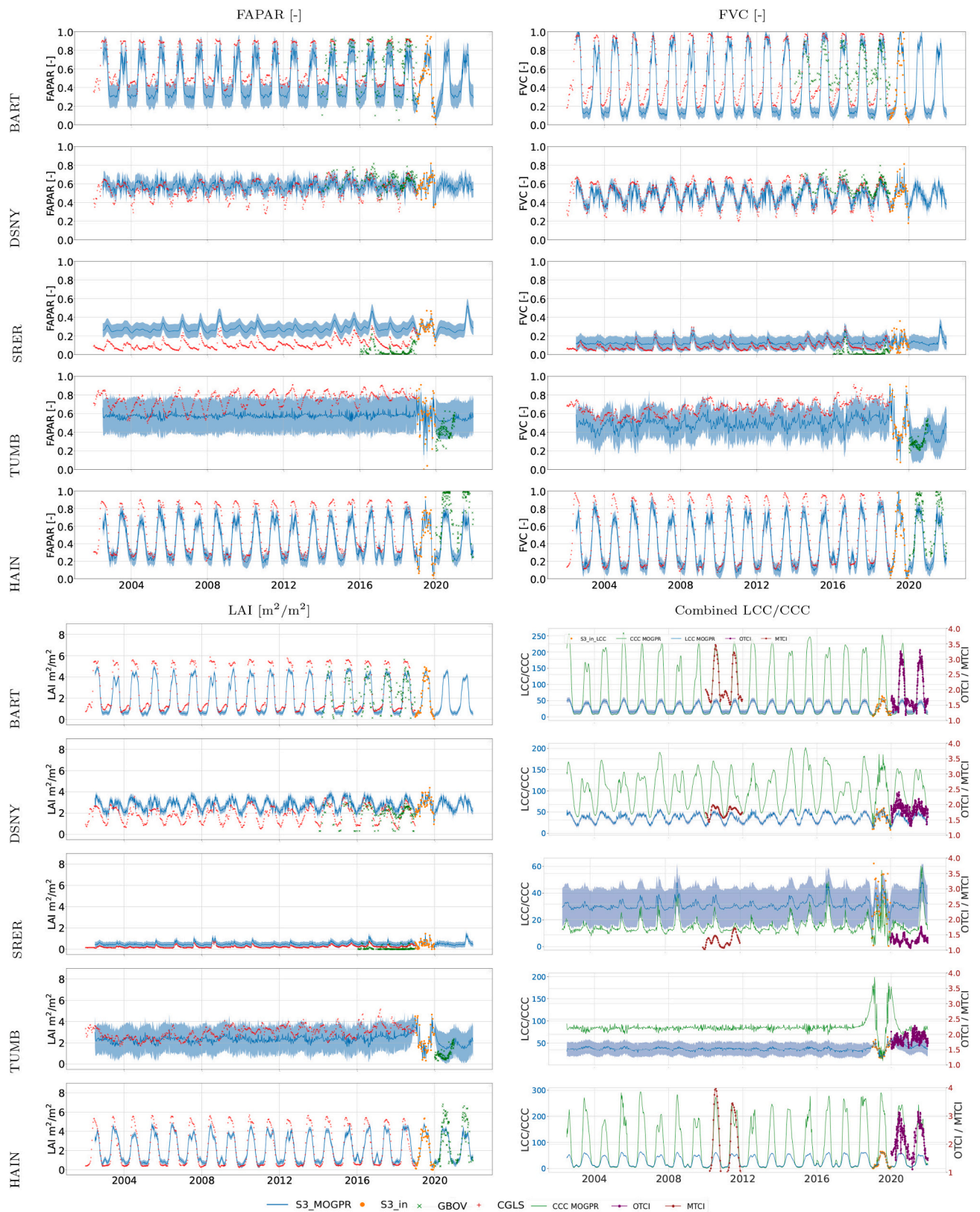## Acknowledgments

Appendix A. Appendix

Fig. A.16. Time series at BART, DSNY, SRER, TUMB and HAIN sites of S3-MOGPR FAPAR, FVC, LAI and LCC reconstructed by the three different predictor variables (preNDVI, preLAI and preFAPAR).

Fig. A.17. Temporal profiles over BART, DSNY, SRER, TUMB and HAIN depicting S3-MOGPR variables for the 2002–2022 window with uncertainties. Also, CGLS, M/OTCI and GBOV in-situ reference measurements are plotted. Yellow dots indicated the training S3 data to the MOGPR algorithm in 2019. PreLAI is used as a predictor variable. The temporal profiles for BLAN, CPER, JERC, and SERC are shown on Fig. 10. (For interpretation of the references to colour in this figure legend, the reader is referred to the web version of this article.)

Table A.8

Average correlation coefficients and averaged normalised error metrics between FAPAR, FVC, LAI-MOGPR, and CGLS data, calculated by using the Fisher method. First, the correlation coefficients for each (R and ρ) were transformed to Fisher Z form, their average was calculated and finally, the inverse Fisher transformation was applied to the averaged Fisher Zs to obtain the mathematically correct $\overline{R}$ and $\overline{\rho}$. This calculation calculated the $\overline{R}$ and $\overline{\rho}$ for each reconstructed variable compared to CGLS, by each predictor variable.

	$\overline{R}$			$\overline{\rho}$		
	preFAPAR	preLAI	preNDVI	preFAPAR	preLAI	preNDVI
FAPAR-MOGPR	0.77	**0.81**	0.61	0.75	**0.76**	0.60
FVC-MOGPR	0.85	**0.91**	0.70	0.80	**0.88**	0.68
LAI-MOGPR	0.80	**0.89**	0.66	0.78	**0.85**	0.66
	Averaged NRMSE			Averaged NMAE		
	preFAPAR	**preLAI**	**preNDVI**	**preFAPAR**	**preLAI**	**preNDVI**
FAPAR-MOGPR	**0.120**	0.123	**0.152**	0.113	**0.111**	0.132
FVC-MOGPR	**0.106**	0.106	**0.137**	0.094	**0.091**	0.122
LAI-MOGPR	**0.084**	0.078	**0.096**	0.070	**0.066**	0.078

Table A.9

Average correlation coefficients and averaged normalised error metrics between LCC-MOGPR and OTCI data, calculated by using the Fisher method. First, the correlation coefficients for each (R and ρ) were transformed to Fisher Z form, their average was calculated, and finally, the inverse Fisher transformation was applied to the averaged Fisher Zs to obtain the mathematically correct R and ρ. This calculation calculated the mean R and ρ for the LCC-OTCI comparison, by each predictor variable.

	$\overline{R}$			$\overline{\rho}$		
	preFAPAR	preLAI	preNDVI	preFAPAR	preLAI	preNDVI
LCC-MOGPR	0.56	**0.78**	0.45	0.57	**0.75**	0.44
	Averaged NRMSE			Averaged NMAE		
	preFAPAR	**preLAI**	**preNDVI**	**preFAPAR**	**preLAI**	**preNDVI**
LCC-MOGPR	0.29	0.20	0.27	0.24	0.16	0.22

References

(Network), N.N.E.O, 2023. Terrestrial Observation System (tos) Site Characterization Report: Domain 14.

Álvarez, M.A., Rosasco, L., Lawrence, N.D., 2012. Kernels for vector-valued functions: a review. Found. Trends Machine Learn. 4, 195. https://doi.org/10.1561/2200000036.

Amin, E., Belda, S., Pipia, L., Szantoi, Z., El Baroudy, A., Moreno, J., Verrelst, J., 2022. Multi-season phenology mapping of nile delta croplands using time series of sentinel-2 and landsat 8 green lai. Remote Sens. 14, 1812. https://doi.org/10.3390/rs14081812.

Bai, G., Dash, J., Brown, L., Meier, C., Lerebourg, C., Ronco, E., Lamquin, N., Bruniquel, V., Clerici, M., Gobron, N., 2019. Gbov (ground-based observation for validation): a copernicus service for validation of vegetation land products. In: IGARSS 2019-2019 IEEE International Geoscience and Remote Sensing Symposium. IEEE, pp. 4592–4594. https://doi.org/10.1109/IGARSS.2019.8898634.

Baret, F., Weiss, M., Lacaze, R., Camacho, F., Makhmara, H., Pacholcyzk, P., Smets, B., 2013. Geov1: Lai and fapar essential climate variables and fcover global time series capitalizing over existing products. Part 1: principles of development and production. Remote Sens. Environ. 137, 299–309. https://doi.org/10.1016/j.rse.2012.12.027.

Barona, E., Ramankutty, N., Hyman, G., Coomes, O.T., 2010. The role of pasture and soybean in deforestation of the Brazilian Amazon. Environ. Res. Lett. 5, 024002 https://doi.org/10.1088/1748-9326/5/2/024002.

Bayat, B., Camacho, F., Nickeson, J., Cosh, M., Bolten, J., Vereecken, H., Montzka, C., 2021. Toward operational validation systems for global satellite-based terrestrial essential climate variables. Int. J. Appl. Earth Obs. Geoinf. 95, 102240.

Belda, S., Pipia, L., Morcillo-Pallarés, P., Rivera-Caicedo, J.P., Amin, E., De Grave, C., Verrelst, J., 2020. DATimeS: a machine learning time series GUI toolbox for gap-filling and vegetation phenology trends detection. Environ. Model Softw. 127, 104666 https://doi.org/10.1016/j.envsoft.2020.104666.

Berger, K., Rivera Caicedo, J.P., Martino, L., Wocher, M., Hank, T., Verrelst, J., 2021. A survey of active learning for quantifying vegetation traits from terrestrial earth observation data. Remote Sens. 13, 287. https://doi.org/10.3390/rs13020287.

Bojanowski, J.S., Sikora, S., Musiał, J.P., Woźniak, E., Dabrowska-Zielińska, K., Slesiński, P., Milewski, T., Łaczyński, A., 2022. Integration of sentinel-3 and modis vegetation indices with era-5 agro-meteorological indicators for operational crop yield forecasting. Remote Sens. 14, 1238. https://doi.org/10.3390/rs14051238.

Bojinski, S., Verstraete, M., Peterson, T.C., Richter, C., Simmons, A., Zemp, M., 2014. The concept of essential climate variables in support of climate research, applications, and policy. Bull. Am. Meteorol. Soc. 95, 1431–1443. https://doi.org/10.1175/BAMS-D-13-00047.1.

Bonilla, E.V., Chai, K., Williams, C., 2007. Multi-task gaussian process prediction. In: Platt, J., Koller, D., Singer, Y., Roweis, S. (Eds.), Advances in Neural Information Processing Systems. Curran Associates, Inc.

Bréda, N.J.J., 2003. Ground-based measurements of leaf area index: a review of methods, instruments and current controversies. J. Exp. Bot. 54, 2403–2417. https://doi.org/10.1093/jxb/erg263 arXiv:14565947.

Brown, M., De Beurs, K., Marshall, M., 2012. Global phenological response to climate change in crop areas using satellite remote sensing of vegetation, humidity and temperature over 26 years. Remote Sens. Environ. 126, 174–183. https://doi.org/10.1016/j.rse.2012.08.009.

Brown, L.A., Dash, J., Lidón, A.L., Lopez-Baeza, E., Dransfeld, S., 2019a. Synergetic exploitation of the sentinel-2 missions for validating the sentinel-3 ocean and land color instrument terrestrial chlorophyll index over a vineyard dominated mediterranean environment. IEEE J. Select. Top. Appl. Earth Observ. Remote Sens. 12, 2244–2251. https://doi.org/10.1109/JSTARS.2019.2899998.

Brown, L.A., Ogutu, B.O., Dash, J., 2019b. Estimating forest leaf area index and canopy chlorophyll content with sentinel-2: an evaluation of two hybrid retrieval algorithms. Remote Sens. 11 https://doi.org/10.3390/rs11151752.

Brown, L.A., Meier, C., Morris, H., Pastor-Guzman, J., Bai, G., Lerebourg, C., Gobron, N., Lanconelli, C., Clerici, M., Dash, J., 2020. Evaluation of global leaf area index and fraction of absorbed photosynthetically active radiation products over north america using copernicus ground based observations for validation data. Remote Sens. Environ. 247, 111935.

Brown, L.A., Fernandes, R., Djamai, N., Meier, C., Gobron, N., Morris, H., Canisius, F., Bai, G., Lerebourg, C., Lanconelli, C., et al., 2021. Validation of baseline and modified sentinel-2 level 2 prototype processor leaf area index retrievals over the United States. ISPRS J. Photogramm. Remote Sens. 175, 71–87.

Buchhorn, M., Smets, B., Bertels, L., Lesiv, M., Tsendbazar, N.E., Masiliunas, D., Linlin, L., Herold, M., Fritz, S., 2020. Copernicus Global Land Service: Land Cover 100m: Collection 3: epoch 2019: Globe (Version V3.0.1). Zenodo. https://doi.org/10.5281/zenodo.3939050.

Buontempo, C., Burgess, S.N., Dee, D., Pinty, B., Thépaut, J.N., Rixen, M., Almond, S., Armstrong, D., Brookshaw, A., Alos, A.L., et al., 2022. The copernicus climate change service: climate science in action. Bull. Am. Meteorol. Soc. 103, E2669–E2687. https://doi.org/10.1175/BAMS-D-21-0315.1.

Burgdorf, A.M., Brönnimann, S., Adamson, G., Amano, T., Aono, Y., Barriopedro, D., Bullón, T., Camenisch, C., Camuffo, D., Daux, V., et al., 2023. Docu-clim: A global documentary climate dataset for climate reconstructions. Sci. Data 10, 402. https://doi.org/10.1038/s41597-023-02303-y.

Caballero, G., Pezzola, A., Winschel, C., Casella, A., Sanchez Angonova, P., Rivera-Caicedo, J.P., Berger, K., Verrelst, J., Delegido, J., 2022. Seasonal mapping of irrigated winter wheat traits in argentina with a hybrid retrieval workflow using sentinel-2 imagery. Remote Sens. 14 https://doi.org/10.3390/rs14184531.

Caballero, G., Pezzola, A., Winschel, C., Sanchez Angonova, P., Casella, A., Orden, L., Salinero-Delgado, M., Reyes-Muñoz, P., Berger, K., Delegido, J., et al., 2023. Synergy

of sentinel-1 and sentinel-2 time series for cloud-free vegetation water content mapping with multi-output gaussian processes. Remote Sens. 15, 1822. https://doi.org/10.3390/rs15071822.

Camacho, F., Cernicharo, J., Lacaze, R., Baret, F., Weiss, M., 2013. Geov1: Lai, fapar essential climate variables and fcover global time series capitalizing over existing products. Part 2: validation and intercomparison with reference products. Remote Sens. Environ. 137, 310–329. https://doi.org/10.1016/j.rse.2013.02.030.

Camps-Valls, G., Verrelst, J., Munoz-Mari, J., Laparra, V., Mateo-Jimenez, F., Gomez-Dans, J., 2016. A Survey on Gaussian Processes for Earth-Observation Data Analysis: A Comprehensive Investigation. https://doi.org/10.1109/MGRS.2015.2510084.

Carroll, M., Townshend, J., Hansen, M., DiMiceli, C., Sohlberg, R., Wurster, K., 2011. Modis vegetative cover conversion and vegetation continuous fields. In: Land Remote Sensing and Global Environmental Change: NASA's Earth Observing System and the Science of ASTER and MODIS, pp. 725–745.

Cavalli, A., Francini, S., McRoberts, R.E., Falanga, V., Congedo, L., De Fioravante, P., Maesano, M., Munafò, M., Chirici, G., Scarascia Mugnozza, G., 2023. Estimating afforestation area using Landsat time series and Photointerpreted datasets. Remote Sens. 15, 923. https://doi.org/10.3390/rs15040923.

Chander, G., Hewison, T.J., Fox, N., Wu, X., Xiong, X., Blackwell, W.J., 2013. Overview of intercalibration of satellite instruments. IEEE Trans. Geosci. Remote Sens. 51, 1056–1080. https://doi.org/10.1109/TGRS.2012.2228654.

Chen, J.M., Black, T.A., 1992. Defining leaf area index for non-flat leaves. Plant Cell Environ. 15, 421–429. https://doi.org/10.1111/j.1365-3040.1992.tb00992.x.

Chen, S., Liu, L., He, X., Liu, Z., Peng, D., 2020. Upscaling from instantaneous to daily fraction of absorbed photosynthetically active radiation (fapar) for satellite products. Remote Sens. 12, 2083. https://doi.org/10.1016/j.jhydrol.2021.126135.

Chen, X., Huang, Y., Nie, C., Zhang, S., Wang, G., Chen, S., Chen, Z., 2022. A long-term reconstructed tropomi solar-induced fluorescence dataset using machine learning algorithms. Sci. Data 9, 427. https://doi.org/10.1038/s41597-022-01520-1.

Chernetskiy, M., Gómez-Dans, J., Gobron, N., Morgan, O., Lewis, P., Truckenbrodt, S., Schmullius, C., 2017. Estimation of fapar over croplands using misr data and the earth observation land data assimilation system (eo-ldas). Remote Sens. 9, 656. https://doi.org/10.3390/rs9070656.

Clevers, J., Bartholomeus, H., Mücher, C., de Wit, A., 2005. Land cover classification with the medium resolution imaging spectrometer (meris). In: Proceedings 24th EARSeL Symposium New Strategies for European Remote Sensing, Dubrovnik, Croatia, 25-27 May 2004, pp. 687–694.

Corey, D.M., Dunlap, W.P., Burke, M.J., 1998. Averaging correlations: expected values and bias in combined Pearson rs and fisher's z transformations. J. Gen. Psychol. 125, 245–261. https://doi.org/10.1080/00221309809595548.

Croft, H., Arabian, J., Chen, J.M., Shang, J., Liu, J., 2020. a. Mapping within-field leaf chlorophyll content in agricultural crops for nitrogen management using Landsat-8 imagery. Precis. Agric. 21, 856–880. https://doi.org/10.1007/s11119-019-09698-y.

Croft, H., Chen, J., Wang, R., Mo, G., Luo, S., Luo, X., He, L., Gonsamo, A., Arabian, J., Zhang, Y., et al., 2020b. The global distribution of leaf chlorophyll content. Remote Sens. Environ. 236, 111479.

Curran, P.J., Dungan, J.L., Gholz, H.L., 1990. Exploring the relationship between reflectance red edge and chlorophyll content in slash pine. Tree Physiol. 7, 33–48. https://doi.org/10.1093/treephys/7.1-2-3-4.33.

Das, S., Roy, S., Sambasivan, R., 2018. Fast gaussian process regression for big data. Big Data Research 14, 12–26. https://doi.org/10.48550/arXiv.1509.05142.

Dash, J., Curran, P., 2007. Evaluation of the meris terrestrial chlorophyll index (MTCI). Adv. Space Res. 39, 100–104.

De Grave, C., Verrelst, J., Morcillo-Pallarés, P., Pipia, L., Rivera-Caicedo, J.P., Amin, E., Belda, S., Moreno, J., 2020. Quantifying vegetation biophysical variables from the Sentinel-3/FLEX tandem mission: evaluation of the synergy of OLCI and FLORIS data sources. Remote Sens. Environ. 251, 112101 https://doi.org/10.1016/j.rse.2020.112101.

Deardorff, J.W., 1978. Efficient prediction of ground surface temperature and moisture, with inclusion of a layer of vegetation. J. Geophys. Res. Oceans 83, 1889–1903. https://doi.org/10.1029/JC083iC04p01889.

Dera, D., Ahmed, S., Bouaynaya, N.C., Rasool, G., 2023. Trustworthy uncertainty propagation for sequential time-series analysis in rnns. IEEE Trans. Knowl. Data Eng. https://doi.org/10.1109/TKDE.2023.3288628.

Devasthale, A., Karlsson, K.G., Andersson, S., Engström, E., 2023. Difference between wmo climate normal and climatology: insights from a satellite-based global cloud and radiation climate data record. Remote Sens. 15, 5598.

Ding, Y., Zheng, X., Jiang, T., Zhao, K., 2015. Comparison and validation of long time serial global geov1 and regional australian modis fractional vegetation cover products over the australian continent. Remote Sens. 7, 5718–5733.

D.Kovács, D.. pyeogpr (zenodo). Zenodo. https://doi.org/10.5281/zenodo.13373838.

Donlon, C., Berruti, B., Buongiorno, A., Ferreira, M.H., Féménias, P., Frerick, J., Goryl, P., Klein, U., Laur, H., Mavrocordatos, C., et al., 2012. The global monitoring for environment and security (gmes) sentinel-3 mission. Remote Sens. Environ. 120, 37–57.

Drusch, M., Moreno, J.F., del Bello, U., Franco, R., Goulas, Y., Huth, A., Kraft, S., Middleton, E.M., Miglietta, F., Mohammed, G.H., Nedbal, L., Rascher, U., Schüttemeyer, D., Verhoef, W., 2017. The FLuorescence EXplorer Mission concept—ESA's earth Explorer 8. IEEE Trans. Geosci. Remote Sens. 55, 1273–1284.

Dubovyk, O., 2017. The role of remote sensing in land degradation assessments: opportunities and challenges. Europ. J. Remote Sens. https://doi.org/10.1080/22797254.2017.1378926.

Elmes, A., Alemohammad, H., Avery, R., Caylor, K., Eastman, J.R., Fishgold, L., Friedl, M.A., Jain, M., Kohli, D., Laso Bayas, J.C., et al., 2020. Accounting for training data error in machine learning applied to earth observations. Remote Sens. 12, 1034.

Estévez, J., Berger, K., Vicent, J., Rivera-Caicedo, J.P., Wocher, M., Verrelst, J., 2021. Top-of-atmosphere retrieval of multiple crop traits using Variational heteroscedastic Gaussian processes within a hybrid workflow. Remote Sens. 13, 1589. https://doi.org/10.3390/rs13081589.

Estévez, J., Salinero-Delgado, M., Berger, K., Pipia, L., Rivera-Caicedo, J.P., Wocher, M., Reyes-Muñoz, P., Tagliabue, G., Boschetti, M., Verrelst, J., 2022. Gaussian processes retrieval of crop traits in Google earth Engine based on Sentinel-2 top-of-atmosphere data. Remote Sens. Environ. 273, 112958 https://doi.org/10.1016/j.rse.2022.112958.

Fang, W., Huang, S., Huang, Q., Huang, G., Wang, H., Leng, G., Wang, L., Guo, Y., 2019. Probabilistic assessment of remote sensing-based terrestrial vegetation vulnerability to drought stress of the loess plateau in China. Remote Sens. Environ. 232, 111290 https://doi.org/10.1016/j.rse.2019.111290.

Fernandes, R., Djamai, N., 2019. Algorithm Theoretical Basis Document Version 1.0 Simplified Level 2 Vegetation Processor–Distributed (sl2p-d) for Estimating Biophysical Variables Using Sentinel-2 Multispectral Imager Data, 1.Canada Centre for Remote Sensing, Ottawa, Canada.

Fernandes, R., Plummer, S., Nightingale, J., Baret, F., Camacho, F., Fang, H., Garrigues, S., Gobron, N., Lang, M., Lacaze, R., LeBlanc, S., Meroni, M., Martinez, B., Nilson, T., Pinty, B., Pisek, J., Sonnentag, O., Verger, A., Welles, J., Weiss, M., Widlowski, J., 2014. Global Leaf Area Index Product Validation Good Practices. Version 2.0. Land Product Validation Subgroup (WGCV/CEOS). https://doi.org/10.5067/doc/ceoswgcv/lpv/lai.002.

Ferrara, R.M., Fiorentino, C., Martinelli, N., Garofalo, P., Rana, G., 2010. Comparison of different ground-based ndvi measurement methodologies to evaluate crop biophysical properties. Ital. J. Agron. 5, 145–154. https://doi.org/10.4081/ija.2010.145.

Fisher, R.A., 1915. Frequency distribution of the values of the correlation coefficient in samples from an indefinitely large population. Biometrika 10, 507–521. https://doi.org/10.2307/2331838.

Fowler, R.L., 1987. Power and robustness in product-moment correlation. Appl. Psychol. Meas. 11, 419–428. https://doi.org/10.1177/014662168701100407.

Fuchs, R., Herold, M., Verburg, P.H., Clevers, J.G.P.W., 2013. A high-resolution and harmonized model approach for reconstructing and analysing historic land changes in Europe. Biogeosciences 10, 1543–1559. https://doi.org/10.5194/bg-10-1543-2013.

Fuster, B., Sánchez-Zapero, J., Camacho, F., García-Santos, V., Verger, A., Lacaze, R., Weiss, M., Baret, F., Smets, B., 2020. Quality assessment of PROBA-V LAI, fAPAR and fCOVER collection 300 m products of Copernicus global land service. Remote Sens. 12 https://doi.org/10.3390/rs12061017.

García-Soria, J.L., Morata, M., Berger, K., Pascual-Venteo, A.B., Rivera-Caicedo, J.P., Verrelst, J., 2024. Evaluating epistemic uncertainty estimation strategies in vegetation trait retrieval using hybrid models and imaging spectroscopy data. Remote Sens. Environ. 310, 114228 https://doi.org/10.1016/j.rse.2024.114228.

Garnesson, P., Mangin, A., Demaria, J., Bretagnon, M., Hembise Fanton d'Andon, O., 2021. First release of the cmems global coastal olci 300 meters chlorophyll-a product. In: EGU General Assembly Conference Abstracts. https://doi.org/10.5194/egusphere-egu21-6239. EGU21–6239.

Gelybó, G., Barcza, Z., Kern, A., Kljun, N., 2013. Effect of spatial heterogeneity on the validation of remote sensing based gpp estimations. Agric. For. Meteorol. 174, 43–53.

Ghent, D., Corlett, G., Göttsche, F.M., Remedios, J., 2017. Global land surface temperature from the along-track scanning radiometers. J. Geophys. Res. Atmos. 122, 12–167. https://doi.org/10.1002/2017JD027161.

Giles, C.L., Lawrence, S., Tsoi, A.C., 2001. Noisy time series prediction using recurrent neural networks and grammatical inference. Mach. Learn. 44, 161–183.

Gitelson, A.A., 2004. Wide dynamic range vegetation index for remote quantification of biophysical characteristics of vegetation. J. Plant Physiol. 161, 165–173. https://doi.org/10.1078/0176-1617-01176.

Gitelson, A.A., Gritz, Y., Merzlyak, M.N., 2003. Relationships between leaf chlorophyll content and spectral reflectance and algorithms for non-destructive chlorophyll assessment in higher plant leaves. J. Plant Physiol. 160, 271–282. https://doi.org/10.1078/0176-1617-00887.

Global Climate Observing System (GCOS), 2022. The 2022 GCOS Essential Climate Variables (ECVs) Requirements (GCOS-245). URL: https://library.wmo.int/records/item/58111-the-2022-gcos-ecvs-requirements-gcos-245.

Global Vegetation Observations (GBOV), 2023. Global Vegetation Observations Algorithm Theoretical Basis Document (ATBD) for RM4, RM6, and RM7 (Version 2.2). URL: https://gbov.acri.fr/public/docs/products/2023-12/GBOV-ATBD-RM4-RM6-RM7_v2.2_Vegetation.pdf.

Gobron, N., Morgan, O., Adams, J., Brown, L.A., Cappucci, F., Dash, J., Lanconelli, C., Marioni, M., Robustelli, M., 2022. Evaluation of sentinel-3A and sentinel-3B ocean land colour instrument green instantaneous fraction of absorbed photosynthetically active radiation. Remote Sens. Environ. 270, 112850 https://doi.org/10.1016/j.rse.2021.112850.

Goldblum, D., Rigg, L.S., 2010. The deciduous forest–boreal forest ecotone. Geogr. Compass 4, 701–717. https://doi.org/10.1111/j.1749-8198.2010.00342.x.

Gomes, V.C.F., Queiroz, G.R., Ferreira, K.R., 2020. An overview of platforms for big earth observation data management and analysis. Remote Sens. 12 https://doi.org/10.3390/rs12081253.

Google Earth Engine, 2023. Google Earth Engine python Api: Introduction to python Api. URL: https://developers.google.com/earth-engine/tutorials/community/intro-to-python-api.

Goovaerts, P., Goovaerts, D.C., 1997. Geostatistics for Natural Resources Evaluation. Oxford University Press, Oxford, England, UK.

Goward, S.N., Markham, B., Dye, D.G., Dulaney, W., Yang, J., 1991. Normalized difference vegetation index measurements from the advanced very high resolution radiometer. Remote Sens. Environ. 35, 257–277. https://doi.org/10.1016/0034-4257(91)90017-Z.

GPy, G., 2012. A Gaussian Process Framework in Python.

Hird, J.N., McDermid, G.J., 2009. Noise reduction of ndvi time series: an empirical comparison of selected techniques. Remote Sens. Environ. 113, 248–258. https://doi.org/10.1016/j.rse.2008.09.003.

Horler, D., Dockray, M., Barber, J., 1983. The red edge of plant leaf reflectance. Int. J. Remote Sens. 4, 273–288. https://doi.org/10.1080/01431168308948546.

Huete, A., Didan, K., Miura, T., Rodriguez, E.P., Gao, X., Ferreira, L.G., 2002. Overview of the radiometric and biophysical performance of the MODIS vegetation indices. Remote Sens. Environ. 83, 195–213.

Johnson, J.E., Laparra, V., Camps-Valls, G., 2019. Accounting for input noise in gaussian process parameter retrieval@articlewang2023intuitive, title={an intuitive tutorial to Gaussian processes regression, author={Wang, Jie, journal={computing in Science & Engineering, year={2023, publisher={IEEE. IEEE Geosci. Remote Sens. Lett. Adv. 1–5 https://doi.org/10.1109/LGRS.2019.2921476.

Joshi, N., Baumann, M., Ehammer, A., Fensholt, R., Grogan, K., Hostert, P., Jepsen, M.R., Kuemmerle, T., Meyfroidt, P., Mitchard, E.T., et al., 2016. A review of the application of optical and radar remote sensing data fusion to land use mapping and monitoring. Remote Sens. 8, 70. https://doi.org/10.3390/rs8010070.

Journel, A., Huijbregts, C., 1978. Mining Geostatistics. Academic Press.

Jutz, S., Milagro-Pérez, M., 2020. Copernicus: The European Earth Observation Programme. Revista de Teledetección, pp. V–XI.

Kaminski, T., Knorr, W., Scholze, M., Gobron, N., Pinty, B., Giering, R., Mathieu, P.P., 2012. Consistent assimilation of MERIS FAPAR and atmospheric CO2 into a terrestrial vegetation model and interactive mission benefit analysis. Biogeosciences 9, 3173–3184. https://doi.org/10.5194/bg-9-3173-2012.

Kang, Y., Ozdogan, M., Gao, F., Anderson, M.C., White, W.A., Yang, Y., Yang, Y., Erickson, T.A., 2021. A data-driven approach to estimate leaf area index for landsat images over the contiguous us. Remote Sens. Environ. 258, 112383.

Khamis, H., 2008. Measures of association: how to choose? J. Diagnost. Med. Sonograph. 24, 155–162. https://doi.org/10.1177/8756479308317006.

Knorr, W., Kaminski, T., Scholze, M., Gobron, N., Pinty, B., Giering, R., Mathieu, P.P., 2010. Carbon cycle data assimilation with a generic phenology model. J. Geophys. Res. Biogeosci. 115 https://doi.org/10.1029/2009JG001119.

Knyazikhin, Y., Martonchik, J., Myneni, R.B., Diner, D., Running, S.W., 1998. Synergistic algorithm for estimating vegetation canopy leaf area index and fraction of absorbed photosynthetically active radiation from modis and misr data. J. Geophys. Res. Atmos. 103, 32257–32275.

Kooistra, L., Berger, K., Brede, B., Graf, L.V., Aasen, H., Roujean, J.L., Machwitz, M., Schlerf, M., Atzberger, C., Prikaziuk, E., et al., 2023. Reviews and syntheses: remotely sensed optical time series for monitoring vegetation productivity. Biogeosci. Discuss. 2023, 1–67. https://doi.org/10.5194/bg-2023-88.

Kotchenova, S.Y., Vermote, E.F., Matarrese, R., Klemm Jr., F.J., 2006. Validation of a vector version of the 6s radiative transfer code for atmospheric correction of satellite data. Part i: path radiance. Appl. Opt. 45, 6762–6774.

Kovács, D.D., Amin, E., Berger, K., Reyes-Muñoz, P., Verrelst, J., 2023a. Untangling the causal links between satellite vegetation products and environmental drivers on a global scale by the granger causality method. Remote Sens. 15, 4956. https://doi.org/10.3390/rs15204956.

Kovács, D.D., Reyes-Muñoz, P., Salinero-Delgado, M., Mészáros, V.I., Berger, K., Verrelst, J., 2023b. Cloud-free global maps of essential vegetation traits processed from the toa sentinel-3 catalogue in google earth engine. Remote Sens. 15, 3404. https://doi.org/10.3390/rs15133404.

Lin, Q., Hu, J., Zhou, Q., Cheng, Y., Hu, Z., Couckuyt, I., Dhaene, T., 2021. Multi-output Gaussian process prediction for computationally expensive problems with multiple levels of fidelity. Knowl.-Based Syst. 227, 107151 https://doi.org/10.1016/j.knosys.2021.107151.

Linderman, M., Zeng, Y., Rowhani, P., 2010. Climate and land-use effects on interannual fAPAR variability from MODIS 250 m data. Photogramm. Eng. Remote. Sens. 76, 807–816. https://doi.org/10.14358/PERS.76.7.807.

Livezey, R.E., Vinnikov, K.Y., Timofeyeva, M.M., Tinker, R., van den Dool, H.M., 2007. Estimation and extrapolation of climate normals and climatic trends. J. Appl. Meteorol. Climatol. 46, 1759–1776.

Long, D., Yan, L., Bai, L., Zhang, C., Li, X., Lei, H., Yang, H., Tian, F., Zeng, C., Meng, X., et al., 2020. Generation of modis-like land surface temperatures under all-weather conditions based on a data fusion approach. Remote Sens. Environ. 246, 111863 https://doi.org/10.1016/j.rse.2020.111863.

Love, B.C., Jones, M., 2012. Bayesian Learning. Springer US, Boston, MA, pp. 415–417. https://doi.org/10.1007/978-1-4419-1428-6_255.

Luo, Y., Melillo, J., Niu, S., Beier, C., Clark, J.S., Classen, A.T., Davidson, E., Dukes, J.S., Evans, R.D., Field, C.B., et al., 2011. Coordinated approaches to quantify long-term ecosystem dynamics in response to global change. Glob. Chang. Biol. 17, 843–854. https://doi.org/10.1111/j.1365-2486.2010.02265.x.

Ma, P., Kang, E.L., 2020. Spatio-temporal data fusion for massive sea surface temperature data from modis and amsr-e instruments. Environmetrics 31, e2594. https://doi.org/10.1002/env.2594.

Mateo-Sanchis, A., Muñoz-Marí, J., Campos-Taberner, M., García-Haro, J., Camps-Valls, G., 2018. Gap filling of biophysical parameter time series with multi-output gaussian processes. In: IGARSS 2018-2018 IEEE International Geoscience and Remote Sensing Symposium. IEEE, pp. 4039–4042. https://doi.org/10.1109/IGARSS.2018.8519254.

McHutchon, A., Rasmussen, C., 2011. Gaussian process training with input noise. Adv. Neural Inf. Proces. Syst. 24.

Moreno, Á., García-Haro, F.J., Martínez, B., Gilabert, M.A., 2014. Noise reduction and gap filling of fAPAR time series using an adapted local regression filter. Remote Sens. 6, 8238–8260. https://doi.org/10.3390/RS6098238.

Mucher, C., Steinnocher, K., Kressler, F., Heunks, C., 2000. Land cover characterization and change detection for environmental monitoring of pan-europe. Int. J. Remote Sens. 21, 1159–1181. https://doi.org/10.1080/014311600210128.

Muradyan, V., Asmaryan, S., Ayvazyan, G., Dell'Acqua, F., 2022. Multidecadal trend analysis of Armenian mountainous grassland and its relationship to climate change using multi-sensor NDVI time-series. Geosciences 12, 412. https://doi.org/10.3390/geosciences12110412.

Mutanga, O., Masenyama, A., Sibanda, M., 2023. Spectral saturation in the remote sensing of high-density vegetation traits: a systematic review of progress, challenges, and prospects. ISPRS J. Photogramm. Remote Sens. 198, 297–309. https://doi.org/10.1016/j.isprsjprs.2023.03.010.

Myneni, R., Williams, D., 1994. On the relationship between fapar and ndvi. Remote Sens. Environ. 49, 200–211. https://doi.org/10.1016/0034-4257(94)90016-7.

Myneni, R., Knyazikhin, Y., Park, T., 2015. MCD15A3H MODIS/Terra+Aqua Leaf Area Index/FPAR 4-Day L4 Global 500m SIN Grid V006.

Nagler, T., Rott, H., Ossowska, J., Schwaizer, G., Small, D., Malnes, E., Luojus, K., Metsämäki, S., Pinnock, S., 2018. Snow cover monitoring by synergistic use of sentinel-3 slstr and sentinel-1 Sar data. In: IGARSS 2018-2018 IEEE International Geoscience and Remote Sensing Symposium. IEEE, pp. 8727–8730. https://doi.org/10.1109/IGARSS.2018.8518203.

National Ecological Observatory Network (NEON), 2023. Bartlett experimental forest - neon. URL: https://www.neonscience.org/field-sites/bart.

Pan, N., Feng, X., Fu, B., Wang, S., Ji, F., Pan, S., 2018. Increasing global vegetation browning hidden in overall vegetation greening: insights from time-varying trends. Remote Sens. Environ. 214, 59–72. https://doi.org/10.1016/j.rse.2018.05.018.

Papagiannopoulou, C., Miralles, D., Dorigo, W.A., Verhoest, N., Depoorter, M., Waegeman, W., 2017. Vegetation anomalies caused by antecedent precipitation in most of the world. Environ. Res. Lett. 12, 074016 https://doi.org/10.1088/1748-9326/aa7145.

Parker, A., Ticehurst, C., Zhou, Z.S., Ward, T., 2021. Application of s-band novasar-1 to bushfires in Australia. In: 2021 IEEE International Geoscience and Remote Sensing Symposium IGARSS. IEEE, pp. 8424–8427.

Pastor-Guzman, J., Brown, L., Morris, H., Bourg, L., Goryl, P., Dransfeld, S., Dash, J., 2020. The sentinel-3 olci terrestrial chlorophyll index (otci): algorithm improvements, spatiotemporal consistency and continuity with the meris archive. Remote Sens. 12, 2652. https://doi.org/10.3390/rs12162652.

Pedelty, J., Devadiga, S., Masuoka, E., Brown, M., Pinzon, J., Tucker, C., Vermote, E., Prince, S., Nagol, J., Justice, C., et al., 2007. Generating a Long-Term Land Data Record From the Avhrr and Modis Instruments, pp. 1021–1025. https://doi.org/10.1109/IGARSS.2007.4422974.

Pipia, L., Muñoz-Marí, J., Amin, E., Belda, S., Camps-Valls, G., Verrelst, J., 2019. Fusing optical and SAR time series for LAI gap filling with multioutput Gaussian processes. Remote Sens. Environ. 235, 111452.

Pipia, L., Amin, E., Belda, S., Salinero-Delgado, M., Verrelst, J., 2021. Green LAI Mapping and Cloud Gap-Filling Using Gaussian Process Regression in Google Earth Engine. https://doi.org/10.3390/rs13030403.

Pipia, L., Belda, S., Franch, B., Verrelst, J., 2022. Trends in satellite sensors and image time series processing methods for crop phenology monitoring. In: Information and Communication Technologies for Agriculture—Theme I: Sensors. Springer, pp. 199–231. https://doi.org/10.1007/978-3-030-84144-7_8.

Poggio, L., Gimona, A., Brown, I., 2012. Spatio-temporal MODIS EVI gap filling under cloud cover: an example in Scotland. ISPRS J. Photogramm. Remote Sens. 72, 56–72. https://doi.org/10.1016/j.ISPRSJPRS.2012.06.003.

Privalsky, V., Gluhovsky, A., 2015. On reconstruction of time series in climatology. Clim. Past Discuss. 11, 4701–4728.

Rasmussen, C.E., 2004. Gaussian processes in machine learning. In: Advanced Lectures on Machine Learning. Springer, pp. 63–71.

Rasmussen, C., Williams, C., 2006. Gaussian Processes for Machine Learning. The MIT Press.

Reiche, J., Verbesselt, J., Hoekman, D., Herold, M., 2015. Fusing landsat and Sar time series to detect deforestation in the tropics. Remote Sens. Environ. 156, 276–293. https://doi.org/10.1016/j.rse.2014.10.001.

Ren, X., Li, X., Ren, K., Song, J., Xu, Z., Deng, K., Wang, X., 2021. Deep learning-based weather prediction: a survey. Big Data Research 23, 100178. https://doi.org/10.1016/j.bdr.2020.100178.

Reyes-Muñoz, P., Pipia, L., Salinero-Delgado, M., Belda, S., Berger, K., Estévez, J., Morata, M., Rivera-Caicedo, J.P., Verrelst, J., 2022. Quantifying fundamental vegetation traits over europe using the sentinel-3 olci catalogue in google earth engine. Remote Sens. 14 https://doi.org/10.3390/RS14061347.

Rodgers, J.L., Nicewander, W.A., 1988. Thirteen ways to look at the correlation coefficient. Am. Stat. 42, 59–66.

Roujean, J.L., Lacaze, R., 2002. Global mapping of vegetation parameters from polder multiangular measurements for studies of surface-atmosphere interactions: a pragmatic method and its validation. J. Geophys. Res. Atmos. 107 https://doi.org/10.1029/2001JD000751. ACL–6.

Salinero-Delgado, M., Estévez, J., Pipia, L., Belda, S., Berger, K., Paredes Gómez, V., Verrelst, J., 2021. Monitoring cropland phenology on google earth engine using gaussian process regression. Remote Sens. 14, 146. https://doi.org/10.3390/rs14010146.

Schmitt, M., Zhu, X.X., 2016. Data fusion and remote sensing: an ever-growing relationship. IEEE Geosci. Remote Sens. Magaz. 4, 6–23. https://doi.org/10.1109/MGRS.2016.2561021.

Schober, P., Boer, C., Schwarte, L.A., 2018. Correlation coefficients: appropriate use and interpretation. Anesth. Analg. 126, 1763–1768. https://doi.org/10.1213/ANE.0000000000002864.

Schramm, M., Pebesma, E., Milenković, M., Foresta, L., Dries, J., Jacob, A., Wagner, W., Mohr, M., Neteler, M., Kadunc, M., et al., 2021. The openeo api–harmonising the use of earth observation cloud services using virtual data cube functionalities. Remote Sens. 13, 1125.

Sedona, R., Cavallaro, G., Jitsev, J., Strube, A., Riedel, M., Benediktsson, J.A., 2019. Remote sensing big data classification with high performance distributed deep learning. Remote Sens. 11, 3056. https://doi.org/10.3390/rs11243056.

Sellers, P.J., Dickinson, R., Randall, D., Betts, A.K., Hall, F.G., Berry, J.A., Collatz, G., Denning, A., Mooney, H.A., Nobre, C.A., et al., 1997. Modeling the exchanges of energy, water, and carbon between continents and the atmosphere. Science 275, 502–509. https://doi.org/10.1126/science.275.5299.502.

Shen, H., Li, X., Cheng, Q., Zeng, C., Yang, G., Li, H., Zhang, L., 2015. Missing information reconstruction of remote sensing data: a technical review. IEEE Geosci. Remote Sens. Magaz. 3, 61–85. https://doi.org/10.1109/MGRS.2015.2441912.

Silver, N.C., Dunlap, W.P., 1987. Averaging correlation coefficients: should fisher's z transformation be used? J. Appl. Psychol. 72, 146. https://doi.org/10.1037/0021-9010.72.1.146.

Snee, R.D., 1977. Validation of regression models: methods and examples. Technometrics 19, 415–428. https://doi.org/10.2307/1267881.

Spearman, C., 1961. The Proof and Measurement of Association Between Two Things. https://doi.org/10.1093/ije/dyq191.

Su, H., Lu, X., Chen, Z., Zhang, H., Lu, W., Wu, W., 2021. Estimating coastal chlorophyll-a concentration from time-series olci data based on machine learning. Remote Sens. 13, 576. https://doi.org/10.3390/rs13040576.

Tang, H., Yu, K., Hagolle, O., Jiang, K., Geng, X., Zhao, Y., 2013. A cloud detection method based on a time series of modis surface reflectance images. Int. J. Digital Earth 6, 157–171. https://doi.org/10.1080/17538947.2013.833313.

Terrascope, 2024. Terrascope: Remote Sensing Data and Services. https://terrascope.be/nl.

Thépaut, J.N., Dee, D., Engelen, R., Pinty, B., 2018. The copernicus programme and its climate change service. In: IGARSS 2018-2018 IEEE International Geoscience and Remote Sensing Symposium. IEEE, pp. 1591–1593. https://doi.org/10.1109/IGARSS.2018.8518067.

Tran, N.N., Huete, A., Nguyen, H., Grant, I., Miura, T., Ma, X., Lyapustin, A., Wang, Y., Ebert, E., 2020. Seasonal comparisons of himawari-8 ahi and modis vegetation indices over latitudinal australian grassland sites. Remote Sens. 12, 2494. https://doi.org/10.3390/rs12152494.

Trenberth, K.E., Dai, A., Van Der Schrier, G., Jones, P.D., Barichivich, J., Briffa, K.R., Sheffield, J., 2014. Global warming and changes in drought. Nat. Clim. Chang. 4, 17–22. https://doi.org/10.1038/nclimate2067.

Trevisiol, F., Mandanici, E., Pagliarani, A., Bitelli, G., 2024. Evaluation of landsat-9 interoperability with sentinel-2 and landsat-8 over europe and local comparison with field surveys. ISPRS J. Photogramm. Remote Sens. 210, 55–68.

UK Multi-Mission Product Archive Facility Infoterra Ltd, Reese, H., Joyce, S., Olsson, H., Curran, P., Dash, J., 2019. Meris Terrestrial Chlorophyll Index (Mtci) Level 3 Composites: Upper North America (Date of citation).

Upreti, D., Huang, W., Kong, W., Pascucci, S., Pignatti, S., Zhou, X., Ye, H., Casa, R., 2019. A comparison of hybrid machine learning algorithms for the retrieval of wheat biophysical variables from sentinel-2. Remote Sens. 11, 481. https://doi.org/10.3390/rs11050481.

Van Der Tol, C., Verhoef, W., Timmermans, J., Verhoef, A., Su, Z., 2009. An integrated model of soil-canopy spectral radiances, photosynthesis, fluorescence, temperature and energy balance. Biogeosciences 6, 3109–3129. https://doi.org/10.5194/bg-6-3109-2009.

Verger, A., Adrià, D., 2022. Copernicus Global Land Operations "Vegetation and Energy", Cglops-1 Algorithm Theoretical Basis Document: Leaf Area Index (Lai), Fraction of Absorbed Photosynthetically Active Radiation (Fapar), Fraction of Green Vegetation Cover (Fcover).

Verger, A., Sánchez-Zapero, J., Weiss, M., Descals, A., Camacho, F., Lacaze, R., Baret, F., 2023. Geov2: Improved smoothed and gap filled time series of lai, fapar and fcover 1 km copernicus global land products. Int. J. Appl. Earth Obs. Geoinf. 123, 103479.

Verhoef, W., Bach, H., 2007. Coupled soil–leaf-canopy and atmosphere radiative transfer modeling to simulate hyperspectral multi-angular surface reflectance and TOA radiance data. Remote Sens. Environ. 109, 166–182. https://doi.org/10.1016/j.rse.2006.12.013.

Vermote, E., Wolfe, R., 2021. Modis/terra Surface Reflectance Daily l2g Global 1km and 500m Sin Grid v061 [Data Set]. https://doi.org/10.5067/MODIS/MOD09GA.061 accessed 2024-06-05.

Vermote, E., Tanré, D., Deuzé, J., Herman, M., Morcrette, J.J., 1997. Second simulation of the satellite signal in the solar spectrum, 6S: an overview. IEEE Trans. Geosci. Remote Sens. 35, 675–686. https://doi.org/10.1109/36.581987.

Verrelst, J., Alonso, L., Camps-Valls, G., Delegido, J., Moreno, J., 2012a. Retrieval of vegetation biophysical parameters using Gaussian process techniques. IEEE Trans. Geosci. Remote Sens. 50, 1832–1843. https://doi.org/10.1109/TGRS.2011.2168962. cited By 26.

Verrelst, J., Muñoz, J., Alonso, L., Delegido, J., Rivera, J.P., Camps-Valls, G., Moreno, J., 2012b. Machine learning regression algorithms for biophysical parameter retrieval: opportunities for sentinel-2 and-3. Remote Sens. Environ. 118, 127–139. https://doi.org/10.1016/j.rse.2011.11.002.

Verrelst, J., Rivera, J.P., Moreno, J., Camps-Valls, G., 2013. Gaussian processes uncertainty estimates in experimental Sentinel-2 LAI and leaf chlorophyll content retrieval. ISPRS J. Photogramm. Remote Sens. 86, 157–167. https://doi.org/10.1016/j.isprsjprs.2013.09.012.

Villacampa-Calvo, C., Zaldívar, B., Garrido-Merchán, E.C., Hernández-Lobato, D., 2021. Multi-class gaussian process classification with noisy inputs. J. Machine Learn. Res. 22, 1696–1747. https://doi.org/10.48550/arXiv.2001.10523.

Von Arx, G., Graf Pannatier, E., Thimonier, A., Rebetez, M., 2013. Microclimate in forests with varying leaf area index and soil moisture: potential implications for seedling establishment in a changing climate. J. Ecol. 101, 1201–1213. https://doi.org/10.1111/1365-2745.12121.

Vuolo, F., Ng, W.T., Atzberger, C., 2017. Smoothing and gap-filling of high resolution multi-spectral time series: example of Landsat data. Int. J. Appl. Earth Obs. Geoinf. 57, 202–213. https://doi.org/10.1016/j.jag.2016.12.012.

Wackernagel, H., 2003. Multivariate Geostatistics: An Introduction with Applications. Springer Science & Business Media.

Wang, J., 2023. An intuitive tutorial to gaussian processes regression. Comp. Sci. Eng. https://doi.org/10.1109/MCSE.2023.3342149.

Wang, J., Delang, C.O., Hou, G., Gao, L., Lu, X., 2021. Net primary production increases in the yangtze river basin within the latest two decades. Glob. Ecol. Conserv. 26, e01497.

Weiss, M., Frederic, B., Smith, G., Jonckheere, I., Coppin, P., 2004. Review of methods for in situ leaf area index (LAI) determination: Part II. Estimation of LAI, errors and sampling. Agric. For. Meteorol. 121, 37–53. https://doi.org/10.1016/j.agrformet.2003.08.001.

Widlowski, J.L., 2010. On the bias of instantaneous fapar estimates in open-canopy forests. Agric. For. Meteorol. 150, 1501–1522. https://doi.org/10.1016/j.agrformet.2010.07.011.

Winkler, K., Fuchs, R., Rounsevell, M., Herold, M., 2021. Global land use changes are four times greater than previously estimated. Nat. Commun. 12, 1–10. https://doi.org/10.1038/s41467-021-22702-2.

Wu, X., Xiao, Q., Wen, J., You, D., Hueni, A., 2019. Advances in quantitative remote sensing product validation: overview and current status. Earth Sci. Rev. 196, 102875 https://doi.org/10.1016/j.earscirev.2019.102875.

Wu, B., Wang, L., Zeng, Y.R., 2022. Interpretable wind speed prediction with multivariate time series and temporal fusion transformers. Energy 252, 123990. https://doi.org/10.1016/j.energy.2022.123990.

Xi, Y., Ren, C., Tian, Q., Ren, Y., Dong, X., Zhang, Z., 2021. Exploitation of time series sentinel-2 data and different machine learning algorithms for detailed tree species classification. IEEE J. Select. Top. Appl. Earth Observ. Remote Sens. 14, 7589–7603. https://doi.org/10.1109/JSTARS.2021.3098817.

Xiao, Z., Liang, S., Wang, T., Liu, Q., 2015. Reconstruction of satellite-retrieved land-surface reflectance based on temporally-continuous vegetation indices. Remote Sens. 7, 9844–9864. https://doi.org/10.3390/RS70809844.

Xiao, Z., Liang, S., Wang, J., Xiang, Y., Zhao, X., Song, J., 2016. Long-time-series global land surface satellite leaf area index product derived from modis and avhrr surface reflectance. IEEE Trans. Geosci. Remote Sens. 54, 5301–5318.

Xiao, Z., Liang, S., Tian, X., Jia, K., Yao, Y., Jiang, B., 2017. Reconstruction of long-term temporally continuous ndvi and surface reflectance from avhrr data. IEEE J. Select. Top. Appl. Earth Observ. Remote Sens. 10, 5551–5568. https://doi.org/10.1109/JSTARS.2017.2744979.

Xu, W., Chen, P., Zhan, Y., Chen, S., Zhang, L., Lan, Y., 2021. Cotton yield estimation model based on machine learning using time series uav remote sensing data. Int. J. Appl. Earth Obs. Geoinf. 104, 102511 https://doi.org/10.1016/j.jag.2021.102511.

Xu, M., Liu, R., Chen, J.M., Liu, Y., Wolanin, A., Croft, H., He, L., Shang, R., Ju, W., Zhang, Y., He, Y., Wang, R., 2022. A 21-year time series of global leaf chlorophyll content maps from MODIS imagery. IEEE Trans. Geosci. Remote Sens. 60, 1–13. https://doi.org/10.1109/TGRS.2022.3204185.

Yan, K., Park, T., Yan, G., Liu, Z., Yang, B., Chen, C., Nemani, R.R., Knyazikhin, Y., Myneni, R.B., 2016. Evaluation of modis lai/fpar product collection 6. Part 2: validation and intercomparison. Remote Sens. 8, 460. https://doi.org/10.3390/rs8060460.

Yan, J., Zhang, G., Ling, H., Han, F., 2022. Comparison of time-integrated ndvi and annual maximum ndvi for assessing grassland dynamics. Ecol. Indic. 136, 108611. https://doi.org/10.1016/j.ecolind.2022.108611.

Yan, K., Wang, J., Peng, R., Yang, K., Chen, X., Yin, G., Dong, J., Weiss, M., Pu, J., Myneni, R.B., 2024. HiQ-LAI: a high-quality reprocessed MODIS leaf area index dataset with better spatiotemporal consistency from 2000 to 2022. Earth Syst. Sci. Data 16, 1601–1622. https://doi.org/10.5194/essd-16-1601-2024.

Yu, W., Li, J., Liu, Q., Zeng, Y., Zhao, J., Xu, B., Yin, G., 2018. Global land cover heterogeneity characteristics at moderate resolution for mixed pixel modeling and inversion. Remote Sens. 10, 856. https://doi.org/10.3390/rs10060856.

Zemp, M., Eggleston, S., Míguez, B.M., Oakley, T., Rea, A., Robbez, M., Tassone, C., 2021. The Status of the Global Climate Observing System 2021: The Gcos Status Report.

Zeng, X., Dickinson, R.E., Walker, A., Shaikh, M., DeFries, R.S., Qi, J., 2000. Derivation and evaluation of global 1-km fractional vegetation cover data for land modeling. J. Appl. Meteorol. Climatol. 39, 826–839. https://doi.org/10.1175/1520-0450(2000)039<0826:DAEOGK>2.0.CO;2.

Zhou, J., Yang, Q., Liu, L., Kang, Y., Jia, X., Chen, M., Ghosh, R., Xu, S., Jiang, C., Guan, K., et al., 2023. A deep transfer learning framework for mapping high spatiotemporal resolution lai. ISPRS J. Photogramm. Remote Sens. 206, 30–48. https://doi.org/10.1016/j.isprsjprs.2023.10.017.